Chemical Geology 615 (2023) 121205

Contents lists available at ScienceDirect

Chemical Geology

journal homepage: www.elsevier.com/locate/chemgeo

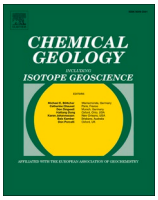

Dating fluid infiltration and deformation in the subducted ultramafic oceanic lithosphere by perovskite geochronology

Francesca Piccoli [a,*], Daniela Rubatto [a], Maria Ovtcharova [b], Jörg Hermann [a], Marcel Guillong [c], Alberto Vitale Brovarone [d,e,f]

[a] Institute of Geological Sciences, Universität Bern, Bern, Switzerland
[b] Department of Mineralogy, University of Geneva, Geneva, Switzerland
[c] Department of Earth Sciences, ETH, Zurich, Switzerland
[d] Dipartimento di Scienze Biologiche, Geologiche e Ambientali (BiGeA), Alma Mater Studiorum Università di Bologna, Bologna, Italy
[e] Institut de Minéralogie, de Physique des Matériaux et de Cosmochimie (IMPMC), Sorbonne Université, Muséum National d'Histoire Naturelle, UMR CNRS 7590, IRD UR206, 75005 Paris, France
[f] Institute of Geosciences and Earth Resources, National Research Council of Italy, Pisa, Italy

ARTICLE INFO

Editor: Balz Kamber

Keywords:
Perovskite U—Pb geochronology
Geochronology of ultramafic rocks
Subduction
Ophicarbonate

ABSTRACT

Carbonated ultramafic rocks (i.e., ophicarbonates) form by peridotite serpentinization and carbonation at the seafloor. Their metamorphic evolution is linked to that of serpentinites, hence dating deformation and metamorphism in ophicarbonates will add constraints to the *P-T-t* history of the subducted ultramafic lithosphere. A potential, yet underexplored, suitable mineral for geochronology in ophicarbonates is perovskite ($CaTiO_3$). We present trace element and geochronological data (LA-ICPMS and ID-TIMS) from perovskite in ophicarbonate rocks and calcite veins from two metamorphic terranes, Lanzo Massif and Val Malenco (Alps). Metamorphic perovskite in ophicarbonates is characterized by enrichment in heavy REE, and strong negative anomalies in Zr and Hf, as well as Sr and Pb, which are attributed to coexistence of a Zr-rich phase and mobilization of these elements by fluids, respectively. Other trace elements broadly reflect the composition of the protolith and allow the distinction of perovskite from mafic and ultramafic rocks.

In the Lanzo Massif, the 49.6 ± 1.0 Ma age of perovskite in shear bands constrains H_2-mediated carbonate reduction and abiotic methane and graphite formation at near peak metamorphic conditions during deformation. Perovskite from Val Malenco is found in calcite veins cutting across serpentinite shear foliation and its age of 48.9 ± 0.5 Ma coincides with a major thrusting and extension event that is distinct in age from the initial nappe stacking. The Val Malenco perovskite age can be reproduced by LA-ICPMS and ID-TIMS and is proposed as a suitable secondary reference material for metamorphic, low U perovskite. These results show that metamorphic perovskite geochronology yields geologically meaningful U—Pb ages and is a viable tool to date deformation and fluid flow in the subducted oceanic lithosphere.

1. Introduction

Ultramafic and mafic lithologies are a major component of the oceanic lithosphere and have a key role in subduction zone chemical geodynamics (Bebout, 2007; Peacock, 2001; Peters et al., 2017; Scambelluri et al., 2019; Ulmer and Trommsdorff, 1995). In addition, hydrated ultramafic rocks (serpentinites) are thermodynamically stable over a sufficiently large range of pressure and temperature (*P-T*) conditions to be able of recording prograde and retrograde subduction related structures (Hermann et al., 2000). However, dating hydration and deformation in ultramafic rocks such as serpentinite is notoriously difficult because of the scarcity of suitable minerals for geochronology. Advances in the analytical methods has allowed expanding the application of (U—Th)/He thermochronology to minerals like magnetite and spinel to retrieve cooling and crystallization ages (Blackburn et al., 2007; Cooperdock and Stockli, 2016, 2018; Schwartz et al., 2020). Nevertheless, this method can only constrain the history of low-grade metamorphic terranes, since the closure temperature for magnetite is 250 ± 40 °C (Schwartz et al., 2020).

Carbonated ultramafic rocks (ophicarbonates hereafter) form by

* Corresponding author.
E-mail address: francesca.piccoli@geo.unibe.ch (F. Piccoli).

https://doi.org/10.1016/j.chemgeo.2022.121205
Received 9 June 2022; Received in revised form 1 November 2022; Accepted 4 November 2022
Available online 9 November 2022

serpentinization and carbonation of exhumed peridotite at the seafloor (Früh-Green et al., 2004; Ludwig et al., 2006). This rock type occurs in present-day oceans and is also abundant in exhumed metamorphic ophiolitic sequences. The metamorphic evolution of ophicarbonates is linked to that of serpentinites (Cannaò et al., 2020; Eberhard and Pettke, 2021; Peng et al., 2021; Scambelluri et al., 2016; Vitale Brovarone et al., 2017), hence dating deformation in metamorphic ophicarbonates may elucidate the *P-T-t* history of the subducted ultramafic lithosphere. Potentially suitable minerals for geochronology in ophicarbonates are calcite and accessory perovskite ($CaTiO_3$). Both minerals have very low U and thus low radiogenic Pb concentrations, while containing a variable amount of initial common-Pb. In these minerals, age determination thus requires variability in Pb/U in the target to define robust data regression in the Tera-Wasserburg diagram (total $^{207}Pb/^{206}Pb$ - $^{238}U/^{206}Pb$) to determine the initial Pb composition. In addition, the application of calcite U—Pb dating is restricted to oceanic or low pressure metamorphic ophicarbonates that did not undergo the calcite-aragonite transition (Coltat et al., 2019; Coogan et al., 2016).

An interesting, yet underexplored alternative to date ophicarbonates is perovskite geochronology. Perovskite is a common accessory mineral in silica-undersaturated magmatic rock (Heaman, 2009; Li et al., 2010; Tappe et al., 2006, 2008, 2011; Wu et al., 2010, 2013b) and skarns (Marincea et al., 2007; Uher et al., 2011), and is also occasionally found in metamorphic ultramafic and mafic rocks (Müntener and Hermann, 1994; Putiš et al., 2015; Shen et al., 2016; Trommsdorff and Evans, 1977). Perovskite is found in metamorphic rock as reaction product, for example by decomposition of magmatic Ti-rich clinopyroxene, but it can also crystallize upon fluid-rock interaction processes such as chlorite-rich metasomatic halo formation around mafic dykes (i.e., blackwalls) (Marfin et al., 2020; Müntener and Hermann, 1994; Shen et al., 2016). Therefore, whenever perovskite occurrence is linked to specific microstructures, U—Pb dating of metamorphic perovskite can provide an age constraint of fluid-related processes and deformation. Moreover, perovskite is a potentially good petrologic indicator of element mobility during fluid flow, because it is a trace element-rich phase hosted in trace element-poor rock (Sun et al., 2014). Yet, trace element data for metamorphic perovskite remain scarce (Li et al., 2014; Putiš et al., 2015; Shen et al., 2016). Few studies already demonstrated that perovskite in serpentinites and associated rodingite blackwalls around mafic dykes can be dated by in situ technique such as laser ablation ICPMS (LA-ICPMS) and SIMS (Li et al., 2014; Shen et al., 2016). Perovskite in ultramafic systems display comparably low U content with respect to available reference materials from magmatic rocks, such as kimberlites (Heaman, 2009; Wu et al., 2010). Since isotopic variations due to chemical composition and crystal structure are known to affect in situ U—Pb dating (Marillo-Sialer et al., 2014; Sun et al., 2022), the accuracy of using magmatic perovskite reference material for metamorphic samples should be tested.

In this contribution, we present a geochemical and geochronological study of perovskite in ophicarbonate rocks and calcite veins from two Alpine metamorphic terranes, Lanzo Massif (Western Alps) and Val Malenco (Central Alps). We show that perovskite from different rock

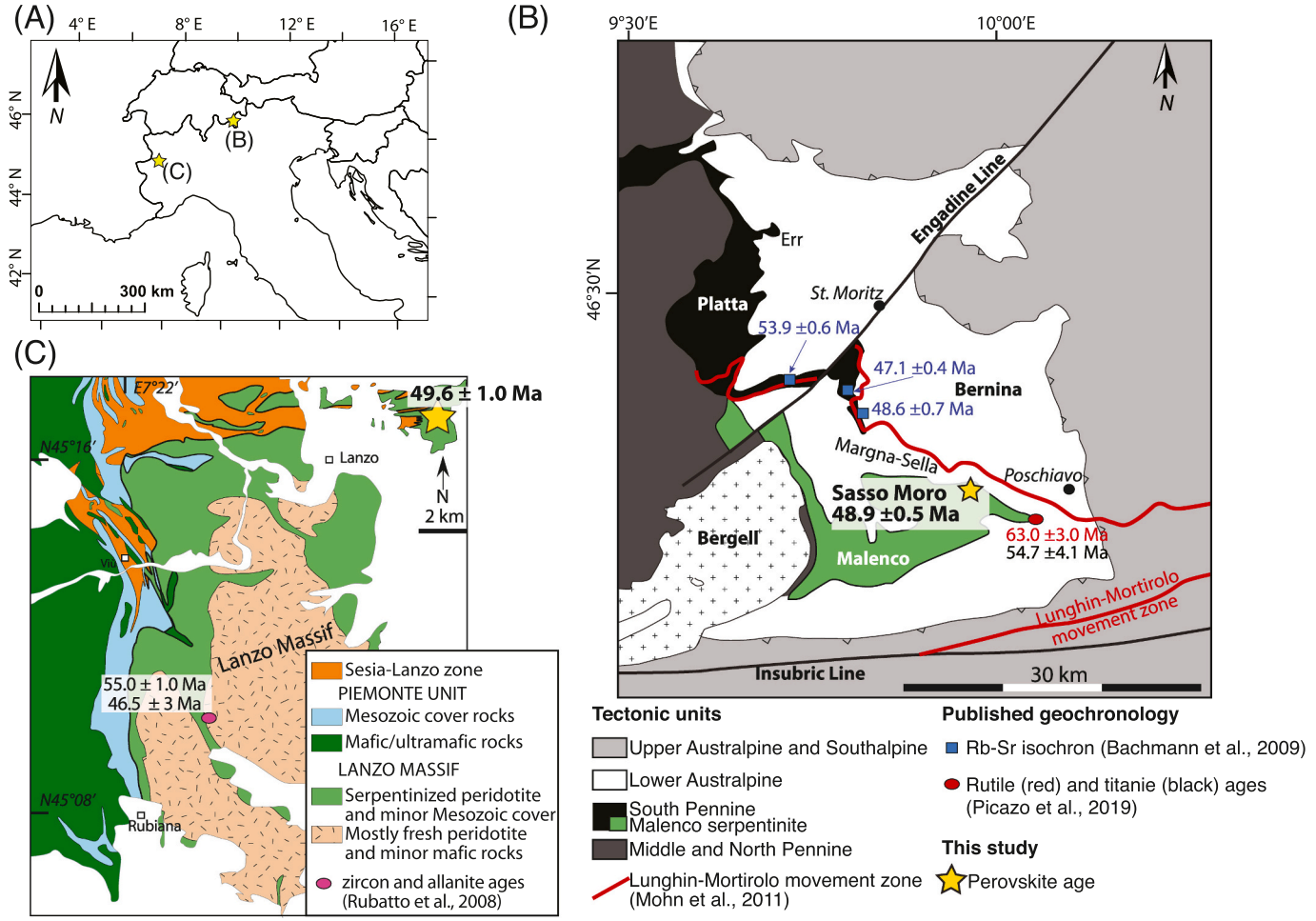

Fig. 1. Geological information on the study areas. A) Geographic setting of the study areas. B) Tectonic map of the Malenco unit and Margna–Sella nappes and the surrounding Austroalpine and South Penninic nappes, along the border between SE of Switzerland and northern Italy (modified after Picazo et al., 2019). C) Simplified geological map of the Lanzo Massif from Vitale Brovarone et al. (2017). In both maps, age constrains from the literature and this study are also reported.

types has distinguishable REE and trace element patterns, mainly reflecting the bulk rock composition. We performed U—Pb in situ analysis by LA-ICPMS in both samples and by isotope dilution-thermal ionization mass spectrometry (ID-TIMS) for the Val Malenco perovskite. Results show that perovskite is a viable geochronological tool to date deformation and fluid flow in the subducted oceanic lithosphere.

2. Geological setting

2.1. Balangero, Lanzo Massif (Italy)

The Lanzo Massif is a large (~150 km^2) ultramafic body located in the internal Western Italian Alps (Fig. 1). The ultramafic rocks belong to a section of oceanic lithosphere exposed at the floor of the Piemonte-Liguria ocean during the Jurassic (Kaczmarek et al., 2008; Pelletier and Müntener, 2006). Part of the body is composed of a core of fresh peridotite (serpentinization <20%) with lherzolitic composition (Piccardo, 2010), surrounded by a fully serpentinized shell with local occurrence of ophicarbonate rocks, a clear indication of seafloor hydrothermal and tectono-sedimentary processes (Coltat et al., 2022; Debret et al., 2013; Lagabrielle et al., 1990; Pelletier and Müntener, 2006). The Alpine high-pressure metamorphism is best recoded in the metagabbros dykes in the internal part of the massif as well as in the ultramafic lithologies at the borders of the massif, where preserved peak parageneses indicate peak metamorphic conditions of 550–620 °C and 2.0–2.5 GPa (Kienast and Pognante, 1988; Pelletier and Müntener, 2006). Prograde to peak metamorphic ages were obtained from recrystallized zircon (55 ± 1 Ma) and allanite (46.5 ± 3.0 Ma) in a metaplagiogranite from the southern part of the Lanzo massif (Rubatto et al., 2008). Zircon ages were interpreted as prograde ages because the most likely source of fluid that acted as agent for dissolution-reprecipitation processes was the surrounding dehydrating serpentinites. Despite being texturally associated with zircon, allanite yielded younger ages. Allanite formation was also attributed to the high-pressure recrystallization because of Na-rich pyroxene inclusions and geochemical features such as high Sr and Ni content and lack of a Eu anomaly. Based on this, the authors proposed that the high-pressure conditions lasted for ~8 million years.

The sample of ophicarbonate studied here is from the northern part of the Lanzo Massif, where a body of ophicarbonate occurs within fully serpentinized peridotite (Giuntoli et al., 2020; Vitale Brovarone et al., 2017). Previous studies showed that the infiltration of reduced H_2-bearing fluids into the ophicarbonates triggered abiotic formation of methane and co-precipitation of graphitic carbon, while enhancing deformation along shear zones (Giuntoli et al., 2020; Vitale Brovarone et al., 2017). Only the minimum metamorphism conditions ($P > 1$GPa, $T > 370$ °C) and relative timing of methanogenesis were inferred by the presence of aragonite inclusions and thermodynamic modelling (Vitale Brovarone et al., 2017). Here we provide further constrain by dating metamorphic perovskite, which occurs in shear bands related to the main deformation event.

2.2. Val Malenco unit (Italy)

The Malenco unit is located in the Eastern Central Italian Alps (Fig. 1). It is structurally situated between the Margna nappe on top, and the Suretta nappe below and is interpreted as a suture zone between the Penninic and the Austroalpine domains (Mohn et al., 2011; Trommsdorff et al., 1993). The Malenco unit is composed of Permian granulite facies lower crust (1.0 GPa and 800–850 °C; (Hermann et al., 1997; Müntener et al., 2000), gabbroic intrusion and ultramafic rocks, the latter representing a portion of subcontinental lithospheric mantle (Müntener and Hermann, 1996). During Jurassic extension, the Malenco crust-mantle section was exhumed to the seafloor of the Piemonte-Liguria ocean and affected by serpentinization and carbonation alteration processes (Hermann and Müntener, 1996; Müntener et al., 2000). The Alpine metamorphic conditions reached ~0.7 GPa and temperatures of ~450–500 °C (Bissig and Hermann, 1999; Hermann and Müntener, 1996; Mellini et al., 1987). The timing of metamorphism is however poorly constrained. The only direct geochronological constraints for Alpine metamorphism in the Malenco unit are from Ar—Ar dating of hornblende from mafic, ultramafic and blackwall rocks (Villa et al., 2000), and from U—Pb dating of rutile and titanite in mafic rocks and blackwalls (Picazo et al., 2019). These studies recognized three groups of ages related to (i) the HP peak at 83–91 Ma (amphibole Ar—Ar age, Villa et al., 2000), (ii) the thermal maximum at 66–73 Ma (amphibole Ar—Ar and rutile U—Pb, Villa et al., 2000; Picazo et al., 2019), and (iii) decompression at 54.7 ± 4.1 Ma (titanite U-Pb; Picazo et al., 2019).

3. Methods

3.1. Sample preparation and characterization

Perovskite grains were prepared as mineral separates, mounted in epoxy or acrylic and polished to expose the minerals. Backscattered electron (BSE) images were acquired with a Zeiss EVO50 SEM (ca. 1 nA beam current, 20 kV accelerating voltage, working distance 10.0–11.0 mm).

3.2. Electron probe micro analysis

Mineral chemistry of silicate minerals and perovskite were determined by wave-length dispersion system using a JEOL JXA 8200 superprobe at the Institute of Geological Sciences, University of Bern, operating with an acceleration voltage of 15 keV, a probe current of 10 nA, 40 s dwell times (including 2 × 10 s of background measurement) and a beam diameter of 1 μm. Spot analyses were measured for each mineral phase present. The mass fractions of element oxides were calibrated using synthetic and natural standards. Analyses are reported in Table S1.

3.3. Trace element analysis

Major, minor and trace elements content in perovskite were acquired by LA-ICPMS with a Resonetics RESOlutionSE 193 nm excimer laser system equipped with a S-155 large volume constant geometry cell (Laurin Technic, Australia) at the Institute of Geological Sciences, University of Bern. Ablation is performed in an atmosphere of pure He (0.4 L min^{-1}) and N_2 (0.003 L min^{-1}) and, immediately after the ablation cell, the aerosol is mixed with Ar (0.86 L min^{-1}). The aerosol is then homogenized by a squid smoothing device and introduced into the plasma of the Agilent 7900 quadrupole ICPMS instrument. A laser repetition rate of 5 Hz and fluence on sample of 4 J cm^{-2} were employed. The ICPMS was tuned on the SRM-NIST612 glass for low oxide production (ThO/Th < 0.2%) and Th/U > 97%. Data acquisition was performed in time-resolved analysis mode, with 30 s background measurement before each analysis. For trace elements, primary standard SRM-NIST 610 was analyzed every 10 samples, secondary standard SRM-NIST 612 every 15 samples to assess the analytic accuracy during the session. Each analysis comprised a series of 34 elements for a total sweep time of 0.626 s. Data are reported in Table S2.

3.4. U-Pb geochronology

In situ U—Pb dating was performed on two LA-ICPMS instruments (single quadrupole in Bern, same as described above for trace elements, and single collector sector field at ETH Zurich) using the same analytical strategy. Primary matrix matched reference material Afrikanda perovskite (AFK, 381.6 ± 1.4 Ma, Wu et al., 2013a) was analyzed every 8 unknowns. Secondary reference material Ice River perovskite (IR, 356.5 ± 1 Ma, Heaman, 2009) every 12 samples. Each analysis comprised

$^{206–207-208}$Pb, ^{232}Th and ^{238}U for a total sweep time of 0.202 s. Mercury 202 and ^{204}Pb were also monitored for interferences. Analytical conditions and instruments detailed information are reported in Table S3; isotopic ratios used for Wetherill and Tera-Wasserburg plots are reported in Table S4. Plots are calculated using IsoplotR (Vermeesch, 2018). The average age and initial lead composition values given represent the maximum likelihood estimate using the algorithm of Ludwig (1998), and the absolute uncertainty is given at 95% confidence interval including overdispersion.

Afrikanda perovskite measured in Bern and in Zurich returned concordant ages that are within uncertainty the same (Fig. 2a,b). For the secondary reference material IR perovskite, the uncorrected data (n = 53) plotted on a Tera-Wasserburg diagram define a regression line with an upper ^{207}Pb/^{206}Pb intercept of 0.696 ± 0.193 and a lower intercept age of 346.6 ± 10.1 Ma (MSWD = 0.74), consistent with what reported by Heaman (2009). The relatively large uncertainty is due to the poor dispersion of the data along the regression. Anchoring the age to a common lead composition of 0.855, based on the bulk Pb evolution model of Stacey and Kramers (1975), returns a more precise age of 353.2 ± 1.8 Ma (MSWD = 0.64). IR perovskite yielded in two different sessions the same common Pb-anchored age (Fig. 2c, d). The accuracy of this age has yet to be confirmed by further studies on the common Pb composition of IR perovskite.

Samples of Val Malenco perovskite were also analyzed by isotope dilution-thermal ionization mass spectrometry (ID-TIMS) at the Department of Earth Sciences of the University of Geneva Perovskite crystals of sample P63 were fragmented using stainless steel tool to achieve fragment size of 50–100 μm. Smaller perovskite crystals of sample P63b were used as single grains. All single grains/fragments were transferred into 3 ml Savilex beakers and cleaned repeatedly in ultrasonic bath, using only deionized ultrapure water. Clean perovskites were transferred into pre-cleaned individual 200 μl Savilex microcapsules, spiked with 5-10 mg EARTHTIME ^{205}Pb-^{233}U-^{235}U tracer solution (Condon et al., 2015) and dissolved in 30 μl 6 N HCl at 210 °C in a Parr bomb for 24 h, to assure complete dissolution and sample-tracer equilibration. Dissolved perovskites were dried down and redissolved in 1 N HBr. Uranium and Pb were separated using single small column (50 μl, AG1-X8 resin) HBr + HCl anion exchange chemistry. The Pb fraction was dried down with 7 μl 0.02 N H_3PO_4 after first column pass, while U was dried down and redissolved in 3 N HCl and passed second time through the columns, assuring purification with HCl before drying down with a drop of H_3PO_4 acid. Both U and Pb were loaded separate on outgassed single Re filaments using 2 μl of Si gel emitter (modified after Gerstenberger and Haase, 1997). Uranium and lead isotope ratios were measured on Thermo Scientific Triton mass spectrometer. The Pb was measured using a dynamic peak-jumping mode on a MasCom secondary electron multiplier (SEM). Pb isotope ratios were corrected for mass fractionation factor of 0.15 ± 0.02% amu, established after repeated

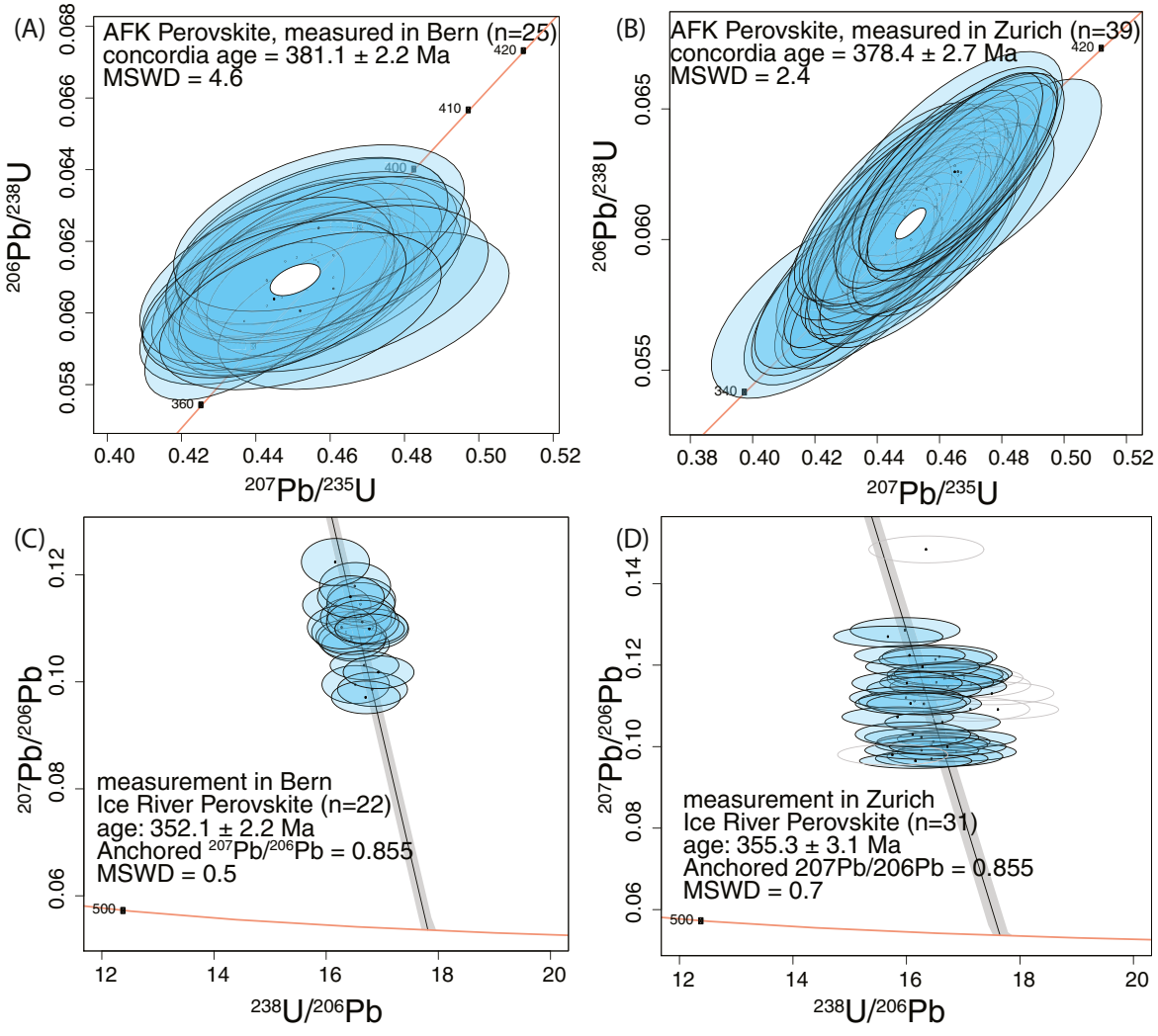

Fig. 2. Concordia (A,B) and Tera-Wasserburg (C,D) diagrams for measured primary (AFK) and secondary (Ice River) perovskite reference materials. Outliers in (D) are shown as light grey, empty ellipses and are excluded from weighted-mean ages and linear regression. Error ellipses represent 2 sigma uncertainties.

measurements of standard SRM 981 and measurements using double spike (EARTHTIME ^{202}Pb-^{205}Pb-^{233}U-^{235}U spike). Uranium isotope ratios were measured as uranium oxide (UO_2) in static mode on Faraday collectors equipped with 10^{13} Ω resistor amplifiers. Measured isotopic ratios were corrected for interferences of $^{238}U^{18}O^{16}O$ on $^{235}U^{16}O_2$ using a $^{18}O/^{16}O$ composition of 0.00205 ± 0.00002. Mass fractionation of U was corrected using a double isotope tracer with a $^{235}U/^{233}U$ of 0.99506 ± 0.00500 and assuming a $^{238}U/^{235}U$ ratio of 137.818 ± 0.045 (Hiess et al., 2012). Total procedural Pb blank for all perovskite using HBr chemistry was estimated to be 1.15 ± 0.25 pg, with a $^{206}Pb/^{204}Pb$ of 18.5 ± 0.13, a $^{207}Pb/^{204}Pb$ of 15.58 ± 0.07 and a $^{208}Pb/^{204}Pb$ of 38.14 ± 0.18 (all 1σ absolute). Total procedural U blanks are measured and a value of 0.01 pg ±50% is used for all data reduction. All analyses were calculated using 1.15 pg of laboratory blank and the remaining common Pb was attributed to initial common Pb. Data reduction and uncertainty propagation were done using Tripoli, YourLab and Isoplot software/excel (Bowring et al., 2011; Ludwig, 1990; McLean et al., 2011; Schmitz and Schoene, 2007). Isochron calculations were performed using IsoplotR (Vermeesch, 2018) with all uncertainties reported in 95% confidence level including overdispersion (without systematic uncertainties associated with the tracer calibration and decay constants). All the results are reported in Table S5.

3.5. MicroRaman spectroscopy

MicroRaman spectroscopy was used to analyze solid and fluid inclusions in perovskite from Balangero. The analyses were carried out on a WITec Alpha 300 MicroRaman at the Department of Biological, Geological, and Environmental Sciences, Bologna University, Italy. The facility is equipped with a 532 nm green laser. The laser power reaching the sample, as measured by the WiTEC TruePower system, was 8 mW for the host perovskite, 40 mW for fluid inclusions, and 2.5 mW for graphite. Ten acquisitions of 25 s were set for perovskite and graphite analyses, whereas 10 acquisitions and 60 s were set for fluid inclusions analyses. Grating was set at 600 grooves/mm.

4. Results

4.1. Sample description

Ophicarbonate rocks from Balangero, Lanzo Massif (45°17,052"N, 7°30′26″E), have been previously described by Vitale Brovarone et al. (2017) and Giuntoli et al. (2020). Here we report the major petrographic features and add details about perovskite occurrence. Sample BAL16–5 is a strongly deformed ophicarbonate (Fig. 3a,b) with a matrix mainly composed by antigorite, oxide and sulfide minerals. Remnants of Ca-carbonate partly replaced by brucite are surrounded by garnet coronas. In thin section, layers rich in diopside and graphite are found along shear planes and shear bands together with garnet and perovskite (Fig. 3b,c,d). Diopside is nearly pure $CaMgSi_2O_6$ and is unzoned. Garnet is an andradite-grossular-uvarovite solid solution with X_{Adr} ranging between 0.87 and 0.98 and X_{Grs} between 0.01 and 0.06 (Table S1). The fraction of uvarovite component reaches up to 0.08. Perovskite crystals are euhedral to subhedral and contain antigorite and chlorite inclusions (Fig. 3c,d). Perovskite composition is stoichiometric $CaTiO_3$. Syn-kinematic, crack-seal textured carbonate veins are also present (Fig. 3a,d). The low carbonate/serpentine ratio likely results from the enhanced carbonate reduction and devolatilization (Giuntoli et al., 2020). The occurrence of diopside, andradite and perovskite along shear bands suggests that these minerals are *syn*-kinematic and formed during reduced fluid infiltration and carbonate reduction. Giuntoli et al. (2020) reported the nucleation of syn-kinematic and syn-reduction second generation of antigorite, graphite, diopside, and andradite along connected creep cavities, i.e. C-C′ shear plans or shear bands. MicroRaman spectroscopy revealed the presence of graphite inclusions in the Balangero perovskite (Fig. 4a) indicating that it grew during or after the H_2-mediated formation of graphite by carbonate reduction. Perovskite also includes CH_4-fluid inclusions (Fig. 4b), presence of which suggests that

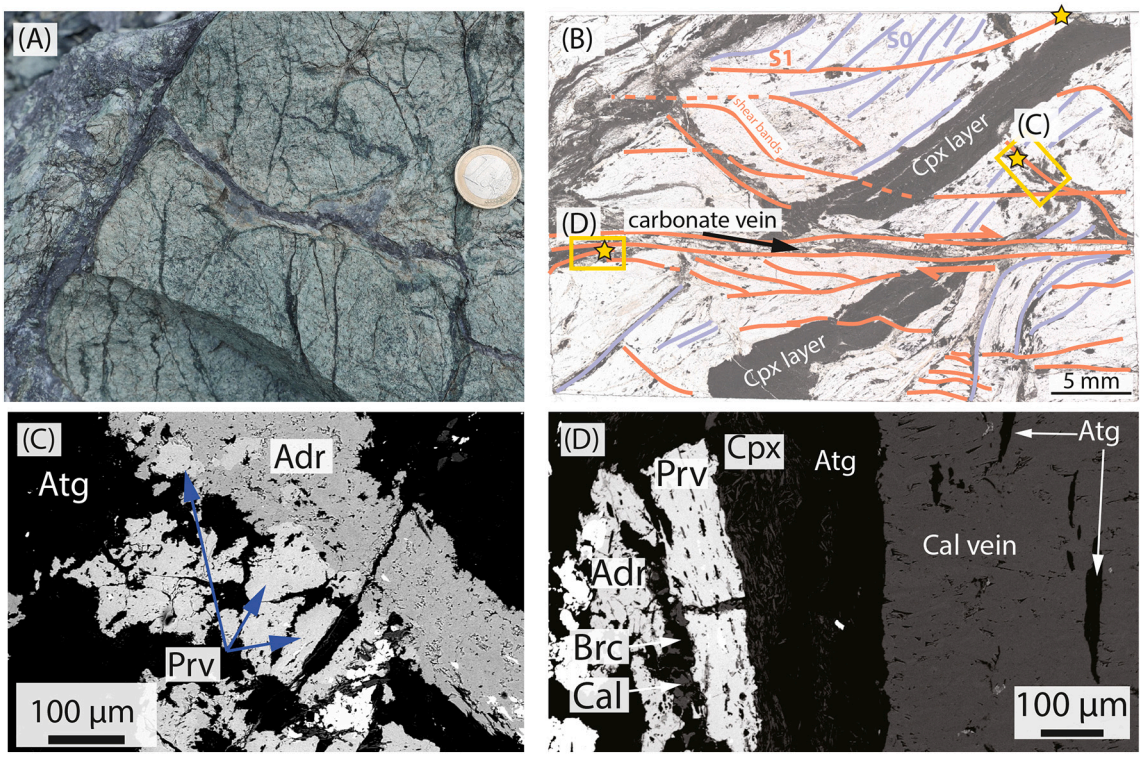

Fig. 3. Field and petrographic images of the studied samples. A) field image of Balangero ophicarbonate; B) thin section scan of Balangero ophicarbonate showing the location of perovskite along shear bands; C) BSE image of perovskite growing with andradite and antigorite; D) diopside, perovskite, andradite and brucite with relict Ca-carbonate.

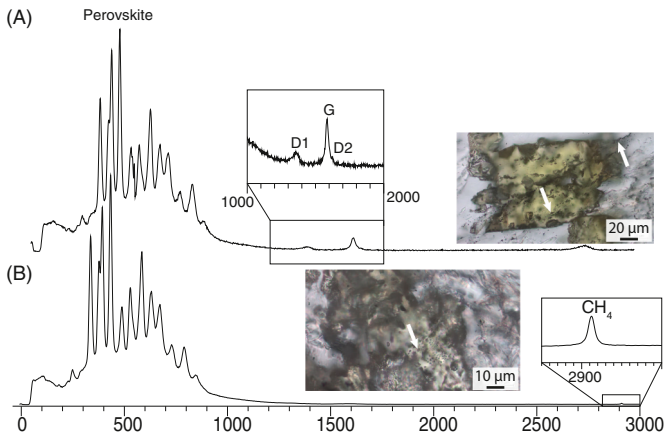

Fig. 4. Microraman spectra of perovskite and included graphite (A) and methane (B) from Balangero. For graphite the G, D1, and D2 band are highlighted. Arrows indicate the position of the analyzed inclusions.

the perovskite formed prior or during the carbonate reduction event.

Perovskite and/or ilmenite veins in the Val Malenco serpentinites have been reported as occurring in the more pyroxene-rich portion of the outcrops (Bedognè et al., 1993). Two samples from the Sasso Moro locality have been investigated in this study. The first sample (P63) comes from the NE ridge of the Sasso Moro and was obtained from a private mineral collection. Field inspection of the area revealed that serpentinites of the Sasso Moro have a rather fertile composition, as indicated by the presence of clinopyroxene and olivine-Ti-clinohumite veins (Fig. 5a,b). Several, partially boudinated, levels of up to a meter thick carbonate layers and carbonate-serpentinite breccias are roughly parallel to the main shear foliation, and occur between 300 and 400 m from the top of the serpentinite body (Fig. 5c). Abundant Ca-carbonate veins, partially rotated and parallelized to the foliation or discordant are also observed (Fig. 5d,e). These veins contain idiomorphic magnetite, ilmenite and more rarely perovskite. Some of the perovskite bearing veins cut across the serpentinite shear foliation (Fig. 5f). A chlorite rich halo often forms around these veins. Sample P63 represent this vein type and contains pseudo-cubic idiomorphic brown crystals of perovskite, sub-mm to mm-size. No ilmenite has been observed and perovskite grains appear unzoned in BSE images (Fig. 5g). Two grain fractions were recovered in the mineral separate: large grains with mm size (P63), and smaller grains sub-mm in size (P63b). One mg of each mineral fraction was used for ID-TIMS measurements. Sample A9089 from Val Malenco (provided by the Natural History Museum of Bern, unknown exact location) is a calcite vein in serpentinite matrix containing pseudo-cubic dark brown/black crystals. Back-scattered images revealed that these crystals are actually ilmenite overgrown by perovskite. This texture hampered a mineral separation for ID-TIMS, but grains were still be used for in situ U—Pb analysis of perovskite.

4.2. Trace element composition of perovskite

All perovskites investigated have a comparable, stoichiometric major element composition. However, as commonly seen in accessory phases, there are notable differences in the trace element composition of the different perovskite samples (Figs. 6,7,8). For comparison, we additionally report the trace element composition of perovskite in chlorite-schists (samples ZS20–28 and ZS20-20A) from the Zermatt-Saas unit. These samples did not contain enough U to be dated, but their trace element composition is still useful for comparison with the other metamorphic perovskite. The petrographic description of the Zermatt-

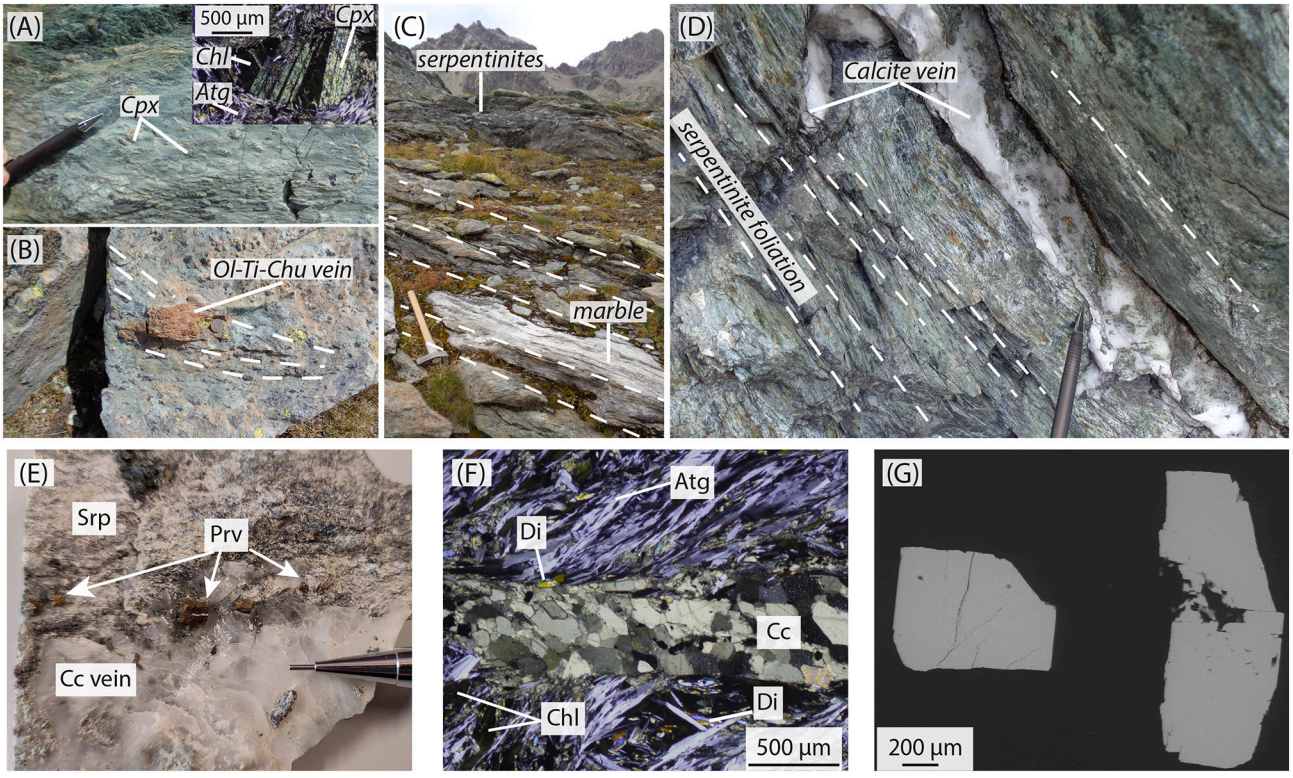

Fig. 5. Field and microstructural observations from Sasso Moro, Val Malenco. A) Clinopyroxene rich serpentinite with photomicrograph in crossed polarized light showing a relict magmatic clinopyroxene. B) Olivine-Ti-clinohumite vein discordant to the shear foliation. C) Marble level parallel to the main top to the South shear foliation in the serpentinites. D) Calcite-chlorite vein parallel and discordant to the foliation. E) Hand specimen of calcite – perovskite vein from Sasso Moro, Val Malenco. F) Crossed polarized light photomicrograph of calcite vein cutting across the serpentinite shear foliation. The thin section is from sample shown in (E). F) BSE image of Val Malenco perovskite crystal separates.

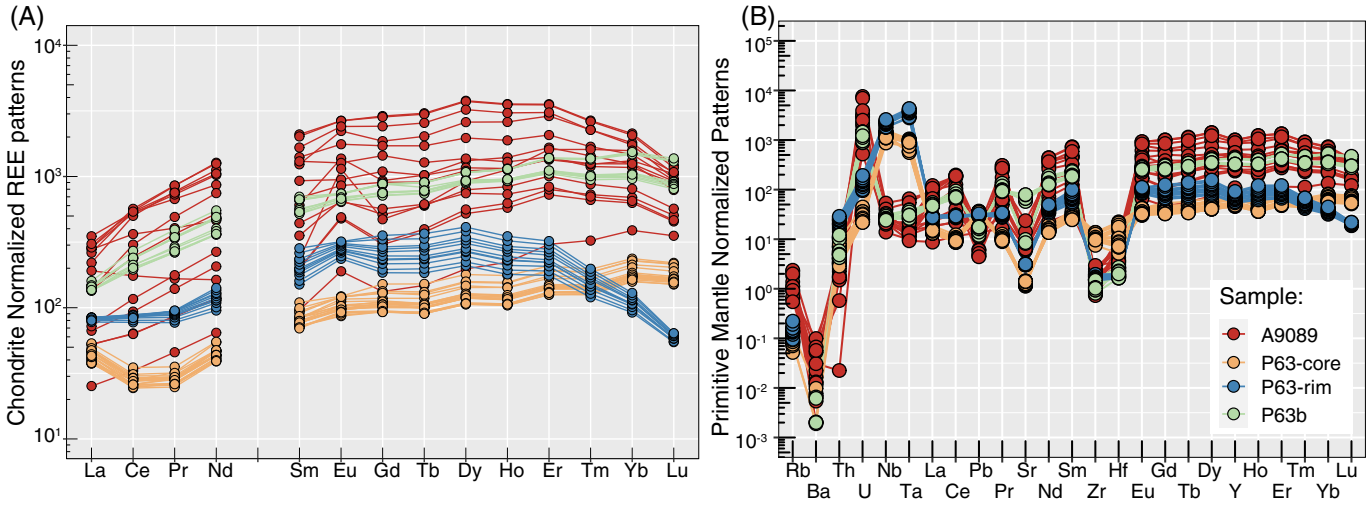

Fig. 6. Trace element composition variability in perovskite from Sasso Moro, Val Malenco. A) Chondrite normalized (Sun and McDonough, 1989) REE patterns of different perovskite samples from Val Malenco. B) Primitive mantle normalized (Sun and McDonough, 1989) trace element patterns of different perovskite samples from Val Malenco.

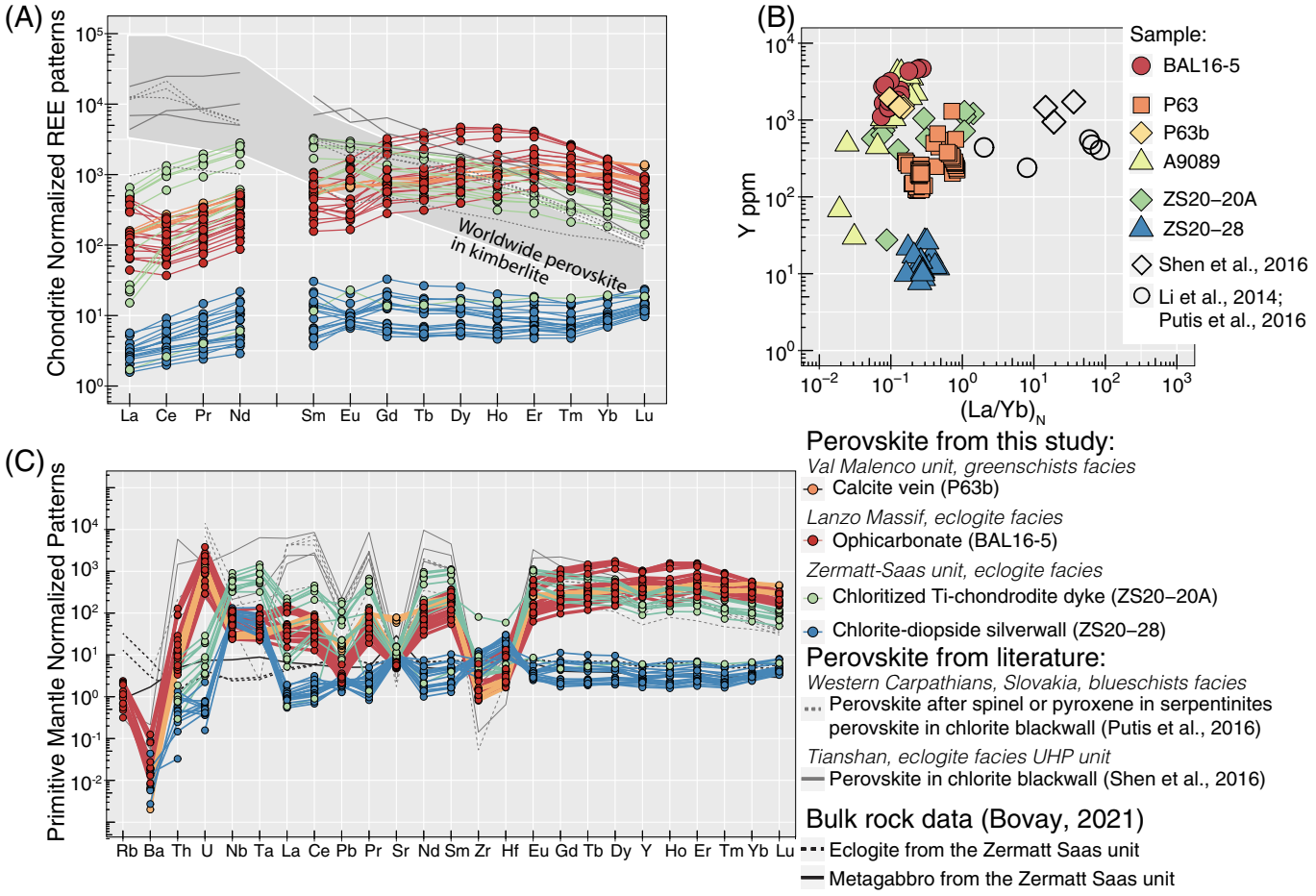

Fig. 7. Trace element composition of metamorphic perovskite. A) Chondrite normalized (Sun and McDonough, 1989) REE patterns of perovskite from different lithologies and localities. Worldwide perovskite in kimberlite is from (Wu et al., 2010, 2013b); B) Normalized La/Yb ratios vs. Y concentrations. C) Primitive mantle normalized (Sun and McDonough, 1989) trace element patterns of perovskite.

Saas samples can be found in the supplementary material.

Among perovskite samples from Val Malenco (P63, P63b and A9089) we observed significant variability in REE and trace element concentrations. Notably, large grain crystals from the aliquot P63 display some heterogeneities between core and rim (Fig. 6a,b) with spoon-shaped LREE pattern, and flat (core) to depleted (rim) HREE. Perovskite from samples P63b and A9089 has generally higher trace element concentrations and displays concave REE patterns with flat or slightly depleted

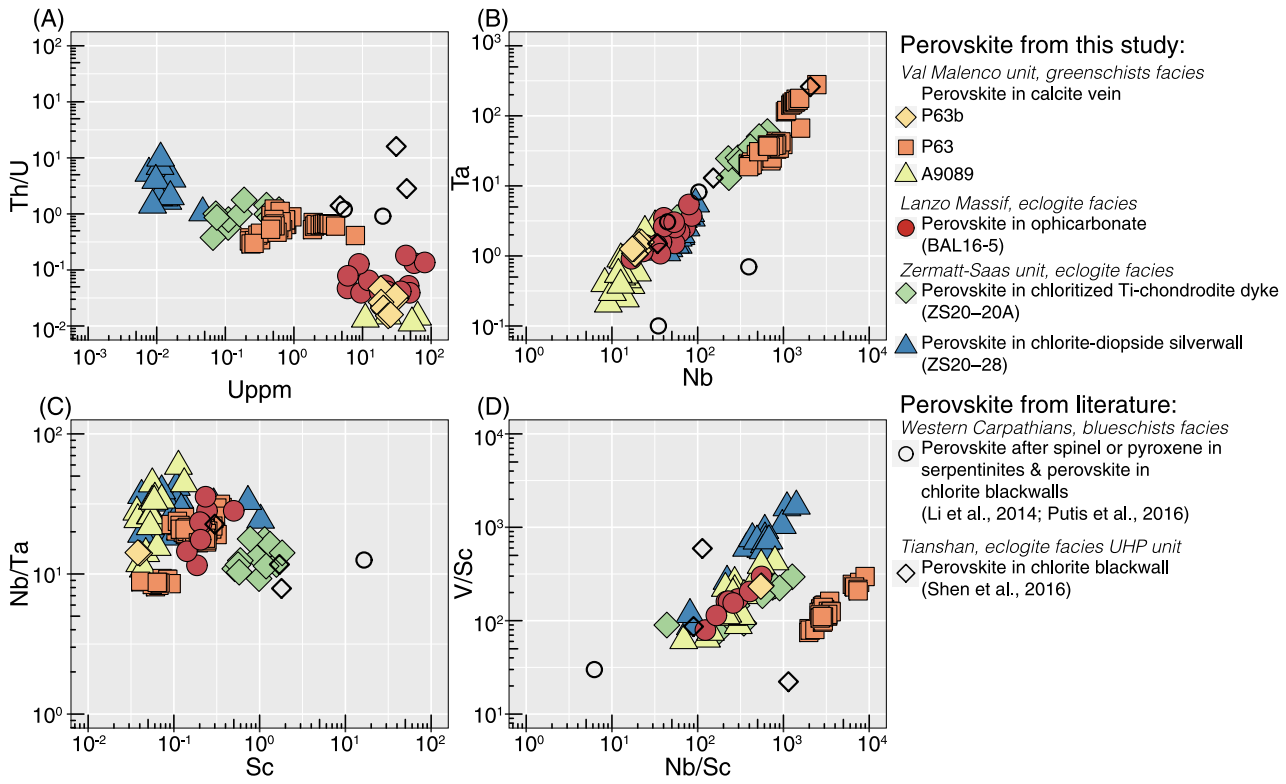

Fig. 8. Elemental plots of different perovskite samples from this study and literature data. A) U concentrations vs. Th/U ratios showing the spread in U content and the characteristic Th/U ratios of perovskite from different lithology; B) Nb vs. Ta concentrations showing a positive correlation for all rock types; C) Sc concentrations vs. Nb/Ta ratios showing the fairly homogenous Nb/Ta ratio for all rock types; and D) Nb/Sc ratios vs. V/Sc ratios showing a positive correlation for all rock types.

HREE (Fig. 6). Similar positive, bell-shaped, REE patterns are observed also in perovskite from chlorite-schists and chloritized Ti-chondrodite dykes from the Zermatt unit (see supplementary material for sample description). However, perovskite in chlorite-schists is poorer in trace elements, and particularly REE, as displayed in the La/Yb vs Y plot (Fig. 7a,b).

Balangero perovskite displays a comparable REE pattern to that of sample P63b from Val Malenco, with positive slope (La_N/Yb_N = 0.12) and no or weak Eu anomaly (Eu/Eu* of 0.5 and 0.8 in the Balangero sample; Fig. 7a). The positive slope of REE pattern in the investigated ophicarbonates and calcite veins is different from the negative slope of perovskite in other ultramafic lithologies such as pyroxenite dykes (Putis et al., 2016; Shen et al., 2016) and chlorite-rich blackwalls (Putis et al., 2016). The relationship between slope of REE patterns and concentration is depicted in the La/Yb vs Y plot (Fig. 7b). In all samples, but the chlorite-schist from Zermatt, perovskites are relatively enriched in trace element compared to chondrite (Fig. 7a) and have similar Y content. Perovskite from the Val Malenco and Balangero ophicarbonates has trace element content above primitive mantle values, with the exception of Ba. Perovskite from both localities has negative Zr and Hf anomalies (absolute concentrations comparable to mantle), similar negative Pb and Sr anomalies (Fig. 7c), and it is quite enriched in Nb and Ta with homogenous Nb/Ta ratios of ca. 20 (Figs. 7c, 8b,c). Vanadium over Sc and Nb/Sc ratios correlate positively (Fig. 8d). In these samples, uranium content ranges between 6 and 80 ppm (Fig. 8a) with a low Th/U between 0.02 and 0.18, with the exception of the large grain aliquot P63 which displays higher Th/U of 0.3 to 1.2, and comparably lower U content (Fig. 8a).

4.3. ID-TIMS dating

Bulk U—Pb isotope dilution analyses were performed for 12 fragments of perovskite sample P63 from Val Malenco by ID-TIMS. Large crystals (P63) of few mm in size were fragmented prior measurements, whereas smaller crystals (P63b) were directly dissolved. All samples contain high level of common Pb, ranging from 2 to 122 pg, and relatively low $^{206}Pb/^{204}Pb$ from 19 to 23. Small crystals have comparable common Pb to large crystals but higher radiogenic Pb (Table S5). Eight aliquots of sample P63, plotted in Tera-Wasserburg space (Fig. 9a) define a single regression with an initial $^{207}Pb/^{206}Pb$ intercept of 0.81744 ± 0.00039 and a lower intercept date of 49.8 ± 5.5 Ma (MSWD = 1.1, n = 8). The isochron defined by 4 aliquots of the small grains (P63b, Fig. 9b) yields a different initial common Pb composition of 0.85023 ± 0.00140 and a lower intercept date of 48.7 ± 0.5 Ma (MSWD = 1.2, n = 4) that is identical to that of P63, within uncertainty.

4.4. LA-ICPMS dating

Sample P63b of Val Malenco perovskite was repeatedly measured at the facility of Bern and ETH Zurich (Fig. 10a). The uncorrected data plotted on a Tera-Wasserburg diagram define a regression with an upper $^{207}Pb/^{206}Pb$ intercept of 0.8508 ± 0.0087 and a lower intercept date of 50.2 ± 2.3 Ma (MSWD = 1.1, n = 133). The LA-ICPMS and ID-TIMS analyses for sample P63b combined define a robust intercept date of 48.9 ± 0.5 Ma, which is the preferred date for this sample (Fig. 10d). Perovskite sample A9089 (Natural History Museum of Bern) yield a date of 51.8 ± 0.7 Ma (MSWD = 1.7, n = 44; Fig. 10b), with an initial $^{207}Pb/^{206}Pb$ composition of 0.8366 ± 0.0062.

Seventy-seven analyses were obtained from Balangero perovskite grains (Fig. 10c). The uncorrected data plotted on a Tera-Wasserburg diagram define a regression with an initial $^{207}Pb/^{206}Pb$ of 0.8892 ± 0.0138 and a lower intercept date of 49.6 ± 1.0 Ma (MSWD = 2, n = 77).

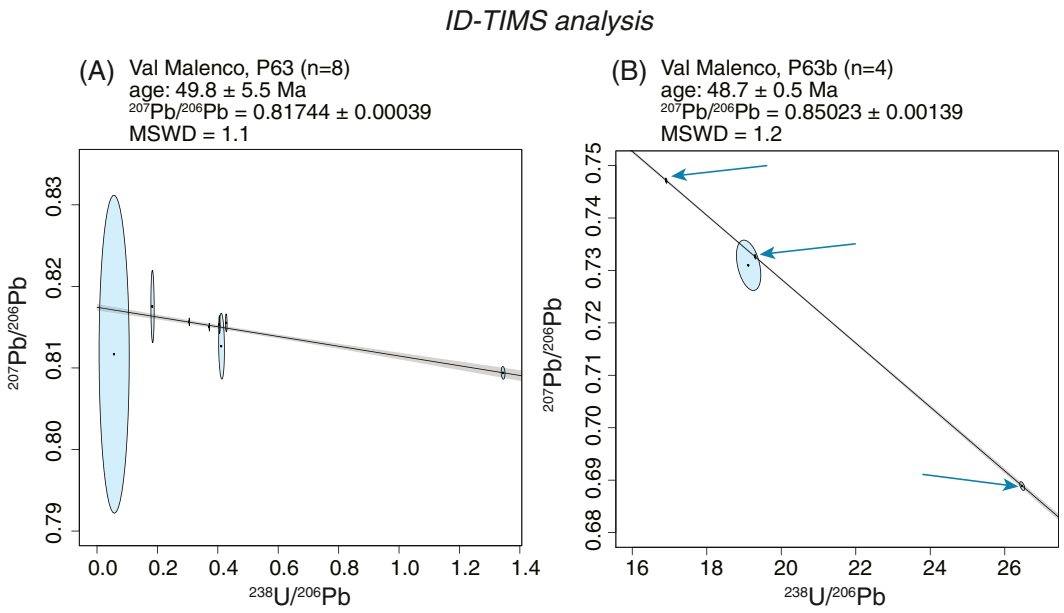

Fig. 9. ID-TIMS U—Pb results for perovskite sample P63 (A) and P63b (B) displayed in Tera-Wasserburg concordia space. Arrows in (B) indicate the data point. Uncertainties on the initial $^{207}Pb/^{206}Pb$ ratios and the intercept ages are at 95% confidence including overdispersion.

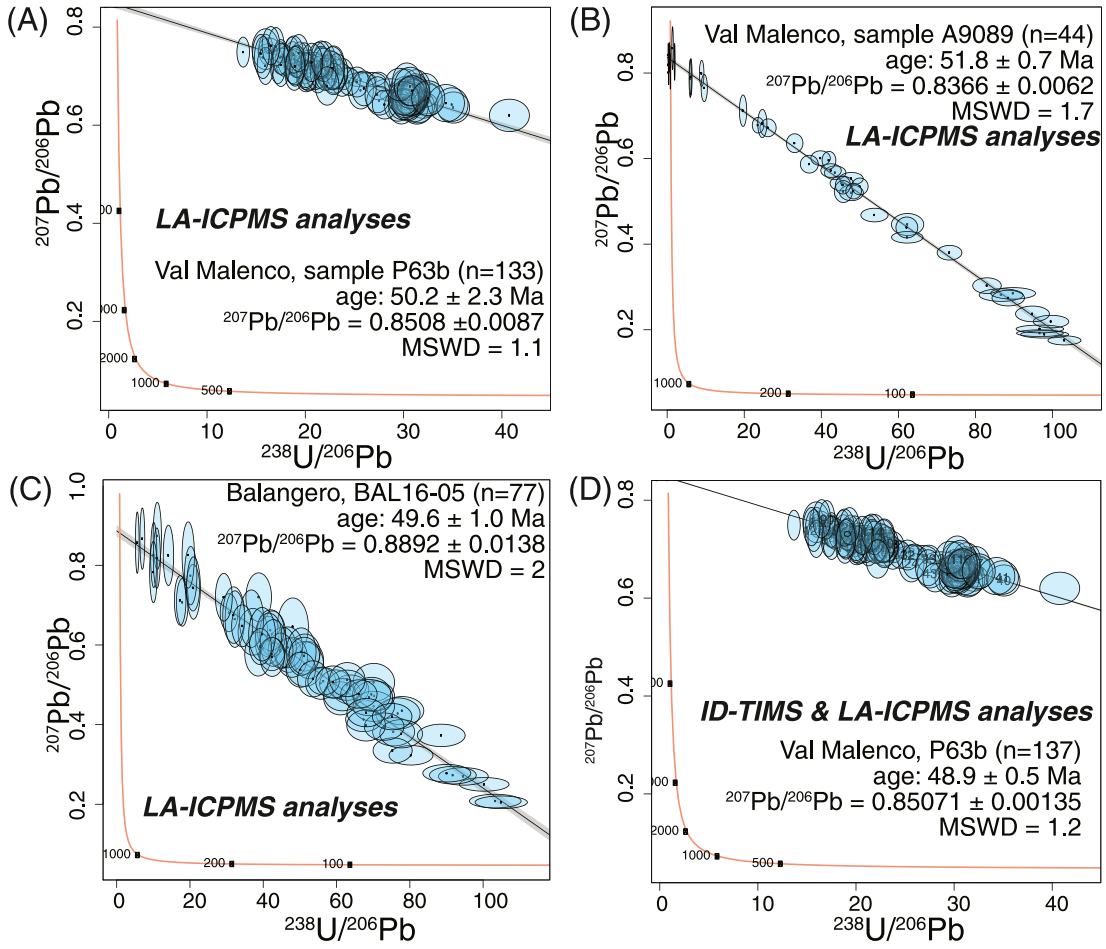

Fig. 10. Tera-Wasserburg diagrams and age determination of different perovskite samples based on uncorrected isotopic ratios: A) sample P63b from Sasso Moro, Val Malenco; B) sample A9089 from Sasso Moro, Val Malenco; C) sample BAL16–05 from Balangero, Lanzo Massif; D) combined ID-TIMS and LA-ICPMS analyses of sample P63b from Sasso Moro, Val Malenco. Error ellipses represent 2 sigma uncertainties.

5. Discussion

5.1. Protolith inheritance and metamorphic fractionation of trace elements

Metamorphic perovskite in blackwalls or as reaction rim on earlier Ti-bearing phases has been previously reported (Li et al., 2014; Müntener and Hermann, 1994; Putis et al., 2016; Shen et al., 2016). To our knowledge, this is the first geochemical and geochronological investigation of metamorphic perovskite in ophicarbonate rocks and calcite vein.

Perovskite from metamorphic samples is clearly distinct from magmatic perovskite, i.e. from kimberlites (e.g. Chakhmouradian and Mitchell, 2000; Tappe et al., 2004), based on its REE pattern. Metamorphic perovskite is relatively depleted in LREE, with REE patterns that are flat or with a positive slope, in contrast to the negative slope typical of perovskite crystallized from a kimberlitic melt (Fig. 7a). With the available data, it can be concluded that perovskite in ophicarbonates and calcite veins, like other metamorphic perovskites, is relatively homogeneous in trace element composition within each sample. From the limited dataset, it is however evident that metamorphic perovskite displays significant variation between ultramafic and mafic lithologies, particularly in REE. The samples investigated in this study and data from literature pertain to perovskite that equilibrated at different metamorphic conditions, spanning from greenschist-facies to ultra-high-pressure conditions (Figs. 7,8). However, the observed variability is not correlated with the metamorphic degree. The variability in trace element composition of perovskite is rather related to the protolith and the partitioning with co-existing phases, i.e. mafic chloritized metagabbros that have an initial MORB composition opposite to ophicarbonates derived from the alteration of peridotite.

Metamorphic perovskite formed in association with mafic rocks, either in the blackwall or as overgrowth on previous Ti-rich phases, displays a fairly wide range of REE patterns (Figs. 6, 7). For perovskite in blackwalls, Shen et al. (2016) attributed the enrichment in REE and other trace element to the fact that the mantle pyroxene was rich in Ti and trace elements, whereas metamorphic diopside and chlorite can host only low amount of trace elements, thus liberating REE for perovskite. In our case study, we observed a large variability in composition even within blackwalls. Perovskite in chlorite-diopside blackwalls ("silverwalls", see Supplementary Material) is strongly depleted in REE (sample ZS20–28) and has trace element patterns that mimic that of eclogites or metagabbros from the same unit (Fig. 7c, Bovay, 2021). Perovskite in chloritized Ti-chondrodite dykes, instead, has similar REE patterns to perovskite forming after spinel or pyroxene (Putis et al., 2016) and perovskite forming in blackwalls around pyroxenite dykes from Tianshan (Shen et al., 2016).

A common feature of perovskite from this study, from Tianshan (Shen et al., 2016) and from western Carpathians (Li et al., 2014; Putiš et al., 2015), is the observed negative anomalies in Zr and Hf, but not in Nb and Ta, which is contrary to what expected if the trace element composition was mainly controlled by the protolith bulk rock. It is plausible that zircon, zirconolite or baddeleyite were stable during chloritization, thus fractionating Zr and Hf. This hypothesis is supported by previous reports of zircon in blackwalls (Bulle et al., 2010; Dubińska et al., 2004), even though a Zr-rich phase was not found in the investigated samples. The preferential partitioning of transitional metals Nb and Ta in Ti-oxide is commonly observed also in other minerals such as ilmenite and rutile and is sometimes used for discrimination diagrams (Pereira et al., 2019; Vieira Duarte et al., 2021). Other transitional metals V and Sc show, however, different behavior. Scandium concentrations are decoupled from Nb/Ta enrichment (Fig. 8a), likely due to preferential partitioning with co-existing silicate phases such as chlorite and diopside. Vanadium, which is compatible in oxide minerals such as magnetite (Dare et al., 2014), varies between tens and hundreds of ppm in perovskite samples (Table S2). When normalized to Sc, a positive correlation between Nb/Sc and V/Sc is observed, which indicates that V is moderately compatible in perovskite. The negative anomaly in Pb (which is mainly common rather than radiogenic) can be explained either by an initial anomaly in the protolith or by preferential mobilization of Pb in the infiltrating fluid. Bulk rock analysis of eclogites and metagabbros from the Zermatt unit do not display a negative Pb anomaly. Consistently, perovskite in the silverwalls also has no Pb anomaly and its trace element pattern is comparable to that of unaltered metabasalt. On the other hand, perovskite in chloritized Ti-chondrodite dyke displays a Pb negative anomaly. Bulk rock data for this rock type are not available, thus we cannot exclude that the negative anomaly is related to fluid metasomatism, rather than protolith.

Perovskite in the Val Malenco calcite veins and Balangero ophicarbonates can be clearly distinguished from metamorphic perovskites in blackwalls both in REE pattern and trace element content: it shows a characteristic enrichment in heavy REE and strong negative anomalies in Zr, Hf, Sr and Pb (Fig. 7a,c). In this case, the negative Sr and Pb anomalies might be explained by the partitioning of Sr and Pb with the co-existing carbonate phase or by mobilization of these elements into fluids. Notably, perovskite crystallization in the Balangero ophicarbonate is associated with consumption of carbonate as proven by microstructural observations (Fig. 3). Therefore in this sample there is no sink for Pb and Sr, suggesting that Sr and Pb were rather mobilized and removed by the fluid. Perovskite in both ophicarbonates and calcite veins has a characteristic low Th/U ratio and variably high U content with respect to metamorphic perovskite in blackwalls (Fig. 8a). This geochemical signature is likely inherited from the oceanic serpentinization and carbonation, where the interaction with the seawater can enrich the bulk rock composition in U, leaving the protolith mantle Th concentration unchanged (Pettke et al., 2018).

In summary the trace element composition of metamorphic perovskite derived from mafic and ultramafic protoliths mainly reflects the composition of the protolith. Selected elements are however sensitive to metamorphic processes: (i) The presence of metamorphic zircon, zirconolite or baddeleyite in blackwalls can be inferred by the negative anomaly in Zr and Hf in perovskite; (ii) U enrichment may reflect bulk U enrichment during oceanic serpentinization; (iii) Perovskite, like other Ti-oxide minerals, can host significant amounts of HFSE and transitional metals such as Nb, Ta and V (Carbonin et al., 2015; Pereira et al., 2019; Toffolo et al., 2017; Vieira Duarte et al., 2021). We found that all samples of metamorphic perovskite have a rather homogenous Nb/Ta ratio and a good correlation between V/Sc and Nb/Sc ratios.

5.2. Validation of U—Pb ages and use of Val Malenco perovskite as secondary reference material

Uranium-Pb dating by LA-ICPMS or SIMS strongly relies on the use of high quality reference material in terms of both chemical and isotopic homogeneity (Chew et al., 2014; Kosler and Sylvester, 2003). Moreover, the use of matrix-matched reference material is required in order to characterize the downhole fractionation (Gregory et al., 2007; Paton et al., 2010). In the case of perovskite, well-characterized, matrix-matched reference materials are available, but they are all magmatic perovskite that are rich in trace elements and U (e.g., Afrikanda and Ice River). Isotopic variations due to chemical composition and crystal structure are known to affect in situ U—Pb dating (Allen and Campbell, 2012; Black et al., 2004; Marillo-Sialer et al., 2014; Sun et al., 2022). For the Tazheran perovskite, for example, it has been proven that in situ ages (SIMS and LA-ICPMS) can be systematically offset with respect to ID-TIMS ages (Sun et al., 2022). Moreover, for low $^{238}U/^{204}Pb$ phases such as perovskite, but also titanite and calcite, it is a common practice to use highly radiogenic reference material to normalize U-poor unknowns that are rich in common Pb. Significant difference in the trace element composition of reference materials and unknowns can cause a slightly different ablation rate between the two (Allen and Campbell, 2012; Marillo-Sialer et al., 2014). Therefore, the downhole fractionation

correction, like other matrix effects, can add to an underestimation of the uncertainty (Marillo-Sialer et al., 2014). This latter aspect has never been investigated for perovskite.

The mm-size crystals and chemical homogeneity in major and trace elements (Figs. 3,6) make the Val Malenco perovskite a potentially good secondary reference material for in situ U—Pb analysis of young, metamorphic perovskites, provided that bulk and in situ ages are consistent. Our repeated analyses of Val Malenco perovskite in two different laboratories validate the obtained in situ age. However, only the small grain fraction (P63b) returned accurate and reproducible results. Analyses on larger grains (fraction P63) did not return a precise in situ age because of the high common Pb content, very low $^{238}U/^{206}Pb$ and, therefore, not enough scatter to define an age with a regression. The ID-TIMS and LA-ICPMS analyses of these two perovskite fractions revealed that they have different Th/U ratios and different initial $^{207}Pb/^{206}Pb$ (Table S5). Despite these differences, they returned the same date within uncertainty, and ID-TIMS and in situ dates are in agreement. This result provides evidence for the accuracy of the in situ dates obtained for both Val Malenco and Balangero perovskite. Furthermore, our results indicate that, (i) within the uncertainty of our measurements, the use of relatively old and radiogenic reference material is appropriate also for young and significantly less radiogenic metamorphic perovskite and (ii) that there is no detectable matrix effect between trace element-poor metamorphic perovskite and trace element-rich magmatic reference material AFK and IR. A different cause of matrix effect during LA-ICPMS analysis was identified in the cubic crystal structure of some Tazheran crystals compared to orthorhombic reference material AFK and IR (Sun et al., 2022).

We conclude that perovskite samples P63b and A9089 characterized in this study can be used as secondary reference material for the analysis of metamorphic perovskite. However, it has to be kept in mind that samples of Val Malenco P63, P63b and A9089, all display different initial $^{207}Pb/^{206}Pb$, which can affect the accuracy of the age obtained (Romer, 2001). In fact, plotting A9089 together with P63b analyzed by LA-ICPMS and ID-TIMS increases the MSWD from 1.2 to 2.2. This indicates that different samples and grain sizes of Val Malenco perovskite are heterogenous in initial $^{207}Pb/^{206}Pb$ and thus a free regression in a Tera-Wasserburg plot is, in this case, the most accurate way to determine an age.

5.3. Significance of the Val Malenco perovskite age

The 48.9 ± 0.5 Ma U-Pb date of the perovskite in carbonate veins from Sasso Moro (P63b) serpentinites is interpreted as a mineral growth age. In the context of previous geochronology, this age clearly postdates the formation of the nappe stack responsible for thrusting the Margna-Sella nappes over the Malenco unit. Geochronological studies conducted in the area include $^{40}Ar/^{39}Ar$ analysis of amphibole, Rb—Sr of white mica, K—Ar,$^{40}Ar/^{39}Ar$ of white mica and biotite, U—Pb of rutile and titanite (Bachmann et al., 2009; Picazo et al., 2019; Price et al., 2018; Siegesmund et al., 2008; Villa et al., 2000). All these geochronometers have different closure temperatures and the age significance has to be evaluated in this context. The most direct geochronological constraints for Alpine metamorphism in the Malenco unit are from $^{40}Ar/^{39}Ar$ dating of hornblende from mafic, ultramafic and blackwall rocks (Villa et al., 2000). Two groups of $^{40}Ar/^{39}Ar$ ages were recognized: 83–91 Ma was related to the pressure dominated peak upon nappe stacking, and 67–73 Ma was attributed to the thermal maximum during exhumation. These ages constrain the first event of crustal thickening, nappe stacking and thrusting top to the West, followed by a late Cretaceous extension with kinematics of top to the East likely leading to the thermal maximum. Our age of 48.9 ± 0.5 Ma for perovskite in carbonate veins as well as the 54.7 ± 4.1 Ma age of titanite from Picazo et al. (2019) are significantly younger than the $^{40}Ar/^{39}Ar$ ages. Therefore, we suggest that perovskite crystallized in the veins during a deformation event related to a later tectonic event, similarly to what was proposed for the interpretation of titanite ages (Picazo et al., 2019). A second event of compression is indeed documented in the first phase of back folding that has a vergence top to the South (Hermann and Müntener, 1996). This deformation phase produces the dominant shear foliation in the serpentinites at the top of the Malenco unit that also affected the Sasso Moro serpentinites (Fig. 5b,c,d, Hermann and Müntener, 1996). The study area is located in the footwall of the Lunghin-Mortirolo movement zone (Fig. 1b), a regional-scale shear zone that separates weakly deformed and cold units in the hangingwall from ductile Alpine deformation in the footwall (Mohn et al., 2011). The Rb—Sr ages of 48–53 Ma from mylonitic metasediments (Bachmann et al., 2009) as well as titanite U—Pb ages of 54.7 ± 4.1 Ma (Picazo et al., 2019) from mafic lithologies, sampled within the Lunghin-Mortirolo movement zone returned ages that within uncertainty agree with our new perovskite age of 48.9 ± 0.5 Ma. Therefore we suggest that the veining event and related perovskite crystallization is likely related to a second main thrusting event, recorded by the top to the south pervasive shear foliation, that is clearly separated in age from the initial nappe stacking. Carbonate veins as well as olivine-Ti-clinohumite veins parallelized and cutting across the serpentinite shear foliation are widespread along the NE flank of the Sasso Moro (Fig. 5b,d). We therefore propose that during this second compression event, partial dehydration of the serpentinites favored C, Ca and Ti mobility which resulted in the formation of carbonate-perovskite veins. The sources of carbonate are most likely the marble and carbonated breccias levels (Fig. 5c), whereas Ti was plausibly sourced from the clinopyroxene rich serpentinite (Fig. 5a).

5.4. Significance of the Balangero perovskite age

The perovskite age of 49.6 ± 1.0 Ma is consistent with the age of metamorphic allanite from an eclogite-facies rock of the Lanzo Massif (46.5 ± 3.0 Ma, Rubatto et al., 2008). Given the microstructural position of perovskite and the presence of methane and graphite inclusions (Figs. 3,4) this age also informs on the timing of carbonate reduction and reduced fluids production during metamorphism. Previous studies (Giuntoli et al., 2020; Vitale Brovarone et al., 2017) already suggested that the infiltration of reduced, H_2-bearing fluids were responsible for carbonate reduction and graphite precipitation following the methanogenic reaction:

$$\mathrm{Atg1 + Arg + 3\,H_2 = Di + 2\,Br + CH_4 + 2H_2O + Gr\ (+ Atg2 + Grt + Prv)} \quad (1)$$

Microstructural evidence presented by Vitale Brovarone et al. (2017) indicates that graphite precipitation occurred in the aragonite stability field, which is crossed during both the prograde and retrograde path. The presence of graphite and CH_4 inclusions in perovskite and its microstructural relationships with *syn*-reduction andradite and clinopyroxene indicate that perovskite formed during the carbonate reduction event. Therefore, the age obtained in this study constrains reaction (1) to near peak conditions, at around 2 GPa and 500 °C.

Reaction (1) requires the infiltration of a reduced H_2 bearing fluid that was likely liberated from the serpentinization reaction of the fresh peridotite of the Lanzo Massif (Vitale Brovarone et al., 2017). Our new age constraint of the reduction reaction suggests that the hydration of fresh peridotites occurred 80–90 km depth, during peak or early exhumation. Availability of free fluid at depth has been suggested by the numerous studies of metasomatic rocks mainly overprinting metasedimentary and/or metamafic lithologies (Bovay et al., 2021; John et al., 2008; Piccoli et al., 2018, 2021; van der Straaten et al., 2012; Vitale Brovarone et al., 2014). Evidence for fluid flow at depth has been more rarely observed in slab ultramafic lithologies (Boutier et al., 2021; Cannaò, 2020; Cannaò et al., 2016; Clément et al., 2019; Kempf et al., 2020; Lafay et al., 2019; Scambelluri et al., 2015; Vitale Brovarone et al., 2020, 2021). To our knowledge, geochronology of metasomatism in ultramafic lithologies has so far been limited to U—Pb on zircon, Rb—Sr on phlogopite (Katayama et al., 2003; Rudnick et al., 1998; Zhang et al.,

2005) or bulk rock *Re*—Os dating (Widom et al., 2003). Perovskite geochronology is therefore a reliable geochronometer to determine the time of fluid flow and deformation in the subducting mantle lithosphere.

6. Conclusion

- In chloritized mafic dykes, metamorphic perovskite trace element composition broadly reflects the pre-metasomatism bulk composition, despite the radical mineralogical change that occurs during chloritization.
- Metamorphic perovskite in chlorite-schists and ophicarbonates preferentially incorporates Nb and Ta with respect to Zr and Hf, which are immobile in high-pressure fluids and are instead fractionated in zircon, zirconolite or baddeleyite.
- No matrix-effect was detected between metamorphic perovskite and AFK or IR perovskite. Therefore, both AFK and IR perovskite can be uses as reference material for LA-ICPMS U—Pb geochronology of metamorphic perovskite. Additionally, perovskite P63b from Val Malenco calcite veins qualifies as good secondary reference material for in situ geochronology of young metamorphic, low-U perovskite.
- Metamorphic perovskite in ophicarbonate rocks and calcite veins records major deformation event and can thus be used to constrain the timing of fluid infiltration and deformation in mantle lithologies: (i) in Val Malenco, calcite-perovskite veins formation (48.9 ± 0.5 Ma) corresponds to the first back folding event, which coincided with dehydration and local mobilization of C, Ca and Ti; (ii) in the Lanzo massif, perovskite crystallized in shear bands and is microstructurally related to a deformation-devolatilization event that occurred at peak conditions, at 49.6 ± 1.0 Ma. This indicates that abiotic methane formation occurred at depth of ca. 80–90 km, with important implications for the deep C cycle.

Declaration of Competing Interest

The authors declare that they have no known competing financial interests or personal relationships that could have appeared to influence the work reported in this paper.

Data availability

Data will be made available on request.

Acknowledgment

This work was supported by the Swiss National Science Foundation grants 200021_191959 to D. Rubatto and 206021_170722 to D. Rubatto and T. Pettke. This work was also supported by the European Research Council (ERC) under the European Union's Horizon 2020 research and innovation program (Grant agreement No. 864045 to A. Vitale Brovarone). The project has benefited from the expertise and the facilities of the BiGeA Raman Lab., University of Bologna. The authors thank Balz Kamber for editorial handling, as well as Larry Heaman and one anonymous reviewer for their constructive comments. We wish to thank B. Hofmann for providing access to the mineral collection of the Natural History Museum of Bern. G. Pearson is thanked for discussion on IR perovskite. P. Kinny and T. Shen are thanked for providing perovskite reference material. F. Piccoli and A. Vitale Brovarone thank R. Compagnoni and G. Cech for the guidance in the field and useful discussion on the occurrences of perovskite in metamorphic rocks. Pietro Nana is thanked for providing samples and information about the Val Malenco perovskites.

Appendix A. Supplementary data

Supplementary data to this article can be found online at https://doi.org/10.1016/j.chemgeo.2022.121205.

References

Allen, C.M., Campbell, I.H., 2012. Identification and elimination of a matrix-induced systematic error in LA–ICP–MS 206Pb/238U dating of zircon. Chem. Geol. 332–333, 157–165. https://doi.org/10.1016/j.chemgeo.2012.09.038.

Bachmann, R., Glodny, J., Oncken, O., Seifert, W., 2009. Abandonment of the South Penninic–Austroalpine palaeosubduction zone, Central Alps, and shift from subduction erosion to accretion: constraints from Rb/Sr geochronology. J. Geol. Soc. 166, 217–231.

Bebout, G.E., 2007. Metamorphic chemical geodynamics of subduction zones. Earth Planet. Sci. Lett. 260, 373–393.

Bedognè, F., Montrasio, A., Sciesa, E., 1993. I minerali della provincia di Sondrio: Valmalenco. éditeur non identifié.

Bissig, T., Hermann, J., 1999. From pre-Alpine extension to Alpine convergence: the example of the southwestern margin of the Margna nappe (Val Malenco, N-Italy). Schweiz. Mineral. Petrogr. Mitt. 79, 363–380.

Black, L.P., Kamo, S.L., Allen, C.M., Davis, D.W., Aleinikoff, J.N., Valley, J.W., Mundil, R., Campbell, I.H., Korsch, R.J., Williams, I.S., Foudoulis, C., 2004. Improved 206Pb/238U microprobe geochronology by the monitoring of a trace-element-related matrix effect; SHRIMP, ID–TIMS, ELA–ICP–MS and oxygen isotope documentation for a series of zircon standards. Chem. Geol. 205, 115–140. https://doi.org/10.1016/j.chemgeo.2004.01.003.

Blackburn, T.J., Stockli, D.F., Walker, J.D., 2007. Magnetite (U–Th)/he dating and its application to the geochronology of intermediate to mafic volcanic rocks. Earth Planet. Sci. Lett. 259, 360–371.

Boutier, A., Vitale Brovarone, A., Martinez, I., Sissmann, O., Mana, S., 2021. High-pressure serpentinization and abiotic methane formation in metaperidotite from the Appalachian subduction, northern Vermont. Lithos 396–397, 106190. https://doi.org/10.1016/j.lithos.2021.106190.

Thomas Bovay, 2021. Origin and pressure-temperature-time-fluid evolution of asubducted volcanoclastic sequence: the Theodul Glacier Unit(Western Alps, Switzerland). PhD thesis.

Bovay, T., Rubatto, D., Lanari, P., 2021. Pervasive fluid-rock interaction in subducted oceanic crust revealed by oxygen isotope zoning in garnet. Contrib. Mineral. Petrol. 176, 1–22.

Bowring, J.F., McLean, N.M., Bowring, S.A., 2011. Engineering cyber infrastructure for U-Pb geochronology: Tripoli and U-Pb_Redux: TRIPOLI AND U-Pb_REDUX SOFTWARE. Geochem. Geophys. Geosyst. 12, n/a-n/a. https://doi.org/10.1029/2010GC003479.

Bulle, F., Bröcker, M., Gärtner, C., Keasling, A., 2010. Geochemistry and geochronology of HP mélanges from Tinos and Andros, cycladic blueschist belt, Greece. Lithos 117, 61–81. https://doi.org/10.1016/j.lithos.2010.02.004.

Cannaò, E., 2020. Boron isotope fractionation in subducted serpentinites: a modelling attempt. Lithos 376–377, 105768. https://doi.org/10.1016/j.lithos.2020.105768.

Cannaò, E., Scambelluri, M., Agostini, S., Tonarini, S., Godard, M., 2016. Linking serpentinite geochemistry with tectonic evolution at the subduction plate-interface: the Voltri Massif case study (Ligurian Western Alps, Italy). Geochim. Cosmochim. Acta 190, 115–133. https://doi.org/10.1016/j.gca.2016.06.034.

Cannaò, E., Scambelluri, M., Bebout, G.E., Agostini, S., Pettke, T., Godard, M., Crispini, L., 2020. Ophicarbonate evolution from seafloor to subduction and implications for deep-Earth C cycling. Chem. Geol. 546, 119626.

Carbonin, S., Martin, S., Tumiati, S., Rossetti, P., 2015. Magnetite from the Cogne serpentinites (Piemonte ophiolite nappe, Italy). Insights into seafloor fluid–rock interaction. Eur. J. Mineral. 27, 31–50.

Chakhmouradian, A.R., Mitchell, R.H., 2000. Occurrence, alteration patterns and compositional variation of perovskite in kimberlites. Can. Mineral. 38, 975–994.

Chew, D.M., Petrus, J.A., Kamber, B.S., 2014. U–Pb LA–ICPMS dating using accessory mineral standards with variable common Pb. Chem. Geol. 363, 185–199. https://doi.org/10.1016/j.chemgeo.2013.11.006.

Clément, M., Padrón-Navarta, J.A., Tommasi, A., 2019. Interplay between fluid extraction mechanisms and antigorite dehydration reactions (Val Malenco, Italian Alps). J. Petrol. 60, 1935–1962. https://doi.org/10.1093/petrology/egz058.

Coltat, R., Branquet, Y., Gautier, P., Campos Rodriguez, H., Poujol, M., Pelleter, E., McClenaghan, S., Manatschal, G., Boulvais, P., 2019. Unravelling the root zone of ultramafic-hosted black smokers-like hydrothermalism from an Alpine analog. Terra Nova 31, 549–561. https://doi.org/10.1111/ter.12427.

Coltat, R., Boulvais, P., Branquet, Y., Richard, A., Tarantola, A., Manatschal, G., 2022. Moho carbonation at an ocean-continent transition. Geology 50, 278–283.

Condon, D.J., Schoene, B., McLean, N.M., Bowring, S.A., Parrish, R.R., 2015. Metrology and traceability of U–Pb isotope dilution geochronology (EARTHTIME Tracer Calibration Part I). Geochim. Cosmochim. Acta 164, 464–480. https://doi.org/10.1016/j.gca.2015.05.026.

Coogan, L.A., Parrish, R.R., Roberts, N.M., 2016. Early hydrothermal carbon uptake by the upper oceanic crust: Insight from in situ U-Pb dating. Geology 44, 147–150.

Cooperdock, E.H., Stockli, D.F., 2016. Unraveling alteration histories in serpentinites and associated ultramafic rocks with magnetite (U-Th)/he geochronology. Geology 44, 967–970.

Cooperdock, E.H., Stockli, D.F., 2018. Dating exhumed peridotite with spinel (U–Th)/he chronometry. Earth Planet. Sci. Lett. 489, 219–227.

Dare, S.A.S., Barnes, S.-J., Beaudoin, G., Méric, J., Boutroy, E., Potvin-Doucet, C., 2014. Trace elements in magnetite as petrogenetic indicators. Mineral. Deposita 49, 785–796. https://doi.org/10.1007/s00126-014-0529-0.

Debret, B., Nicollet, C., Andreani, M., Schwartz, S., Godard, M., 2013. Three steps of serpentinization in an eclogitized oceanic serpentinization front (Lanzo Massif–Western Alps). J. Metamorph. Geol. 31, 165–186.

Dubińska, E., Bylina, P., Kozłowski, A., Dörr, W., Nejbert, K., Schastok, J., Kulicki, C., 2004. U–Pb dating of serpentinization: hydrothermal zircon from a metasomatic rodingite shell (Sudetic ophiolite, SW Poland). Chem. Geol. 203, 183–203. https://doi.org/10.1016/j.chemgeo.2003.10.005.

Eberhard, L., Pettke, T., 2021. Antigorite dehydration fluids boost carbonate mobilisation and crustal CO2 outgassing in collisional orogens. Geochim. Cosmochim. Acta 300, 192–214.

Früh-Green, G.L., Connolly, J.A., Plas, A., Kelley, D.S., Grobéty, B., 2004. Serpentinization of oceanic peridotites: implications for geochemical cycles and biological activity. In: The Subseafloor Biosphere at Mid-ocean Ridges, 144, pp. 119–136.

Gerstenberger, H., Haase, G., 1997. A highly effective emitter substance for mass spectrometric Pb isotope ratio determinations. Chem. Geol. 136, 309–312. https://doi.org/10.1016/S0009-2541(96)00033-2.

Giuntoli, F., Vitale Brovarone, A., Menegon, L., 2020. Feedback between high-pressure genesis of abiotic methane and strain localization in subducted carbonate rocks. Sci. Rep. 10, 1–15.

Gregory, C.J., Rubatto, D., Allen, C.M., Williams, I.S., Hermann, J., Ireland, T., 2007. Allanite micro-geochronology: a LA-ICP-MS and SHRIMP U–Th–Pb study. Chem. Geol. 245, 162–182.

Heaman, L.M., 2009. The application of U–Pb geochronology to mafic, ultramafic and alkaline rocks: an evaluation of three mineral standards. Chem. Geol. 261, 43–52.

Hermann, J., Müntener, O., 1996. Extension-related structures in the Malenco-Margna-system: Implications for paleogeography and consequences for rifting and Alpine tectonics. Schweiz. Mineral. Petrogr. Mitt. 76, 501–520.

Hermann, J., Müntener, O., Scambelluri, M., 2000. The importance of serpentinite mylonites for subduction and exhumation of oceanic crust. Tectonophysics 327 (3–4), 225–238.

Hermann, J., Müntener, O., Trommsdorff, V., Hansmann, W., Piccardo, G.B., 1997. Fossil crust-to-mantle transition, Val Malenco (Italian Alps). J. Geophys. Res. Solid Earth 102, 20123–20132.

Hiess, J., Condon, D.J., McLean, N., Noble, S.R., 2012. 238U/235U systematics in terrestrial uranium-bearing minerals. Science 335 (6076), 1610–1614.

John, T., Klemd, R., Gao, J., Garbe-Schoenberg, C.-D., 2008. Trace-element mobilization in slabs due to non steady-state fluid–rock interaction: constraints from an eclogite-facies transport vein in blueschist (Tianshan, China). Lithos 103, 1–24.

Kaczmarek, M.-A., Müntener, O., Rubatto, D., 2008. Trace element chemistry and U–Pb dating of zircons from oceanic gabbros and their relationship with whole rock composition (Lanzo, Italian Alps). Contrib. Mineral. Petrol. 155, 295–312.

Katayama, I., Muko, A., Iizuka, T., Maruyama, S., Terada, K., Tsutsumi, Y., Sano, Y., Zhang, R.Y., Liou, J.G., 2003. Dating of zircon from Ti-clinohumite–bearing garnet peridotite: Implication for timing of mantle metasomatism. Geology 31, 713–716.

Kempf, E.D., Hermann, J., Reusser, E., Baumgartner, L.P., Lanari, P., 2020. The role of the antigorite+ brucite to olivine reaction in subducted serpentinites (Zermatt, Switzerland). Swiss J. Geosci. 113, 1–36.

Kienast, J., Pognante, U., 1988. Chloritoid-bearing assemblages in eclogitised metagabbros of the Lanzo peridotite body (western Italian Alps). Lithos 21, 1–11.

Kosler, J., Sylvester, P., 2003. Present trends and the future of zircon in geochronology: laser ablation ICPMS. Rev. Mineral. Geochem. 53, 243–275. https://doi.org/10.2113/0530243.

Lafay, R., Baumgartner, L.P., Putlitz, B., Siron, G., 2019. Oxygen isotope disequilibrium during serpentinite dehydration. Terra Nova 31, 94–101. https://doi.org/10.1111/ter.12373.

Lagabrielle, Y., Fudral, S., Kienast, J.-R., 1990. La couverture océanique des ultrabasites de Lanzo (Alpes occidentales): arguments lithostratigraphiques et pétrologiques. Geodin. Acta 4, 43–55. https://doi.org/10.1080/09853111.1990.11105199.

Li, Q.-L., Li, X.-H., Liu, Y., Wu, F.-Y., Yang, J.-H., Mitchell, R., 2010. Precise U–Pb and Th–Pb age determination of kimberlitic perovskites by secondary ion mass spectrometry. Chem. Geol. 269, 396–405.

Li, X.-H., Putiš, M., Yang, Y.-H., Koppa, M., Dyda, M., 2014. Accretionary wedge harzburgite serpentinization and rodingitization constrained by perovskite U/Pb SIMS age, trace elements and Sm/Nd isotopes: Case study from the Western Carpathians, Slovakia. Lithos 205, 1–14.

Ludwig, K., 1990. ISOPLOT for MS. DOS: a plotting and regression program for radiogenic isotopic data for IBMPC compatible computers, Version 2.11. US. Geol. Survey Open File Report 88–557.

Ludwig, K.R., 1998. On the treatment of concordant uranium-lead ages. Geochim. Cosmochim. Acta 62, 665–676.

Ludwig, K.A., Kelley, D.S., Butterfield, D.A., Nelson, B.K., Früh-Green, G., 2006. Formation and evolution of carbonate chimneys at the lost City Hydrothermal Field. Geochim. Cosmochim. Acta 70, 3625–3645.

Marfin, A.E., Ivanov, A.V., Kamenetsky, V.S., Abersteiner, A., Yakich, T.Y., Dudkin, T.V., 2020. Contact metamorphic and metasomatic processes at the Kharaelakh intrusion, Oktyabrsk deposit, Norilsk-Talnakh ore district: application of LA-ICP-MS dating of perovskite, apatite, garnet, and titanite. Econ. Geol. 115, 1213–1226.

Marillo-Sialer, E., Woodhead, J., Hergt, J., Greig, A., Guillong, M., Gleadow, A., Evans, N., Paton, C., 2014. The zircon 'matrix effect': evidence for an ablation rate control on the accuracy of U–Pb age determinations by LA-ICP-MS. J. Anal. At. Spectrom. 29, 981–989. https://doi.org/10.1039/C4JA00008K.

Marincea, Ş., Dumitraş, D., Fransolet, A., 2007. The association spurrite–perovskite in the inner exoskarn zone from Cornet Hill (Metaliferi Mountains, Romania). Sciences 118.

McLean, N.M., Bowring, J.F., Bowring, S.A., 2011. An algorithm for U-Pb isotope dilution data reduction and uncertainty propagation: U-Pb ALGORITHM. Geochem. Geophys. Geosyst. 12, n/a-n/a. https://doi.org/10.1029/2010GC003478.

Mellini, M., Trommsdorff, V., Compagnoni, R., 1987. Antigorite polysomatism: behaviour during progressive metamorphism. Contrib. Mineral. Petrol. 97, 147–155.

Mohn, G., Manatschal, G., Masini, E., Müntener, O., 2011. Rift-related inheritance in orogens: a case study from the Austroalpine nappes in Central Alps (SE-Switzerland and N-Italy). Int. J. Earth Sci. 100, 937–961.

Müntener, O., Hermann, J., 1994. Titanian andradite in a metapyroxenite layer from the Malenco ultramafics (Italy): implications for Ti-mobility and low oxygen fugacity. Contrib. Mineral. Petrol. 116, 156–168.

Müntener, O., Hermann, J., 1996. The Val Malenco lower crust–upper mantle complex and its field relations (Italian Alps). Schweiz. Mineral. Petrogr. Mitt. 76, 475–500.

Müntener, O., Hermann, J., Trommsdorff, V., 2000. Cooling history and exhumation of Lower-Crustal Granulite and Upper Mantle (Malenco, Eastern Central Alps). J. Petrol. 41, 175–200. https://doi.org/10.1093/petrology/41.2.175.

Paton, C., Woodhead, J.D., Hellstrom, J.C., Hergt, J.M., Greig, A., Maas, R., 2010. Improved laser ablation U-Pb zircon geochronology through robust downhole fractionation correction. Geochem. Geophys. Geosyst. 11.

Peacock, S.M., 2001. Are the lower planes of double seismic zones caused by serpentine dehydration in subducting oceanic mantle? Geology 29, 299–302.

Pelletier, L., Müntener, O., 2006. High-pressure metamorphism of the Lanzo peridotite and its oceanic cover, and some consequences for the Sesia–Lanzo zone (northwestern Italian Alps). Lithos 90, 111–130. https://doi.org/10.1016/j.lithos.2006.01.006.

Peng, W., Zhang, L., Tumiati, S., Brovarone, A.V., Hu, H., Cai, Y., Shen, T., 2021. Abiotic methane generation through reduction of serpentinite-hosted dolomite: implications for carbon mobility in subduction zones. Geochim. Cosmochim. Acta 311, 119–140.

Pereira, I., Storey, C., Darling, J., Lana, C., Alkmim, A.R., 2019. Two billion years of evolution enclosed in hydrothermal rutile: Recycling of the São Francisco Craton Crust and constraints on gold remobilisation processes. Gondwana Res. 68, 69–92.

Peters, D., Bretscher, A., John, T., Scambelluri, M., Pettke, T., 2017. Fluid-mobile elements in serpentinites: Constraints on serpentinisation environments and element cycling in subduction zones. Chem. Geol. 466, 654–666.

Pettke, T., Kodolányi, J., Kamber, B.S., 2018. From ocean to mantle: new evidence for U-cycling with implications for the HIMU source and the secular Pb isotope evolution of Earth's mantle. Lithos 316, 66–76.

Picazo, S.M., Ewing, T.A., Müntener, O., 2019. Paleocene metamorphism along the Pennine–Austroalpine suture constrained by U–Pb dating of titanite and rutile (Malenco, Alps). Swiss J. Geosci. 112, 517–542.

Piccardo, G.B., 2010. The Lanzo peridotite massif, Italian Western Alps: Jurassic rifting of the Ligurian Tethys. Geol. Soc. Lond., Spec. Publ. 337, 47–69. https://doi.org/10.1144/SP337.3.

Piccoli, F., Vitale Brovarone, A., Ague, J.J., 2018. Field and petrological study of metasomatism and high-pressure carbonation from lawsonite eclogite-facies terrains, Alpine Corsica. Lithos 304, 16–37. https://doi.org/10.1016/j.lithos.2018.01.026.

Piccoli, F., Ague, J.J., Chu, X., Tian, M., Brovarone, A.V., 2021. Field-based evidence for intra-slab high-permeability channel formation at eclogite-facies conditions during subduction. Geochem. Geophys. Geosyst. https://doi.org/10.1029/2020GC009520.

Price, J.B., Wernicke, B.P., Cosca, M.A., Farley, K.A., 2018. Thermochronometry across the Austroalpine-Pennine Boundary, Central Alps, Switzerland: Orogen-perpendicular normal fault slip on a major "overthrust" and its implications for orogenesis. Tectonics 37, 724–757.

Putiš, M., Yang, Y.-H., Koppa, M., Dyda, M., Šmál, P., 2015. U/Pb LA–ICP–MS age of metamorphic–metasomatic perovskite from serpentinized harzburgite in the Meliata Unit at Dobšiná, Slovakia: Time constraint of fluid–rock interaction in an accretionary wedge. Acta Geol. Slovaca 7, 63–71.

Putis, M., Yang, Y.-H., Vaculovic, T., Koppa, M., Li, X.-H., Uher, P., 2016. Perovskite, reaction product of a harzburgite with Jurassic-cretaceous accretionary wedge fluids (Western Carpathians, Slovakia): evidence from the whole-rock and mineral trace element data. Geol. Carpath. 67, 135.

Romer, R.L., 2001. Lead incorporation during crystal growth and the misinterpretation of geochronological data from low-238U/204Pb metamorphic minerals. Terra Nova 13, 258–263. https://doi.org/10.1046/j.1365-3121.2001.00348.x.

Rubatto, D., Müntener, O., Barnhoorn, A., Gregory, C., 2008. Dissolution-reprecipitation of zircon at low-temperature, high-pressure conditions (Lanzo Massif, Italy). Am. Mineral. 93, 1519–1529.

Rudnick, R., Ireland, T., Gehrels, G., Irving, A., Chesley, J., Hanchar, J., 1998. Dating mantle metasomatism: U-Pb geochronology of zircons in cratonic mantle xenoliths from Montana and Tanzania. In: Presented at the International Kimberlite Conference: Extended Abstracts, pp. 754–756.

Scambelluri, M., Pettke, T., Cannaò, E., 2015. Fluid-related inclusions in Alpine high-pressure peridotite reveal trace element recycling during subduction-zone dehydration of serpentinized mantle (Cima di Gagnone, Swiss Alps). Earth Planet. Sci. Lett. 429, 45–59. https://doi.org/10.1016/j.epsl.2015.07.060.

Scambelluri, M., Bebout, G.E., Belmonte, D., Gilio, M., Campomenosi, N., Collins, N., Crispini, L., 2016. Carbonation of subduction-zone serpentinite (high-pressure ophicarbonate; Ligurian Western Alps) and implications for the deep carbon cycling. Earth Planet. Sci. Lett. 441, 155–166.

Scambelluri, M., Cannaò, E., Gilio, M., 2019. The water and fluid-mobile element cycles during serpentinite subduction. A review. EJM 31, 405–428. https://doi.org/10.1127/ejm/2019/0031-2842.

Schmitz, M.D., Schoene, B., 2007. Derivation of isotope ratios, errors, and error correlations for U-Pb geochronology using ^{205} Pb- ^{235} U-(^{233} U)-spiked isotope dilution thermal ionization mass spectrometric data: U-PB ISOTOPE RATIO DERIVATION. Geochem. Geophys. Geosyst. 8 https://doi.org/10.1029/2006GC001492 n/a-n/a.

Schwartz, S., Gautheron, C., Ketcham, R.A., Brunet, F., Corre, M., Agranier, A., Pinna-Jamme, R., Haurine, F., Monvoin, G., Riel, N., 2020. Unraveling the exhumation history of high-pressure ophiolites using magnetite (U-Th-Sm)/He thermochronometry. Earth Planet. Sci. Lett. 543, 116359.

Shen, T., Wu, F., Zhang, L., Hermann, J., Li, X., Du, J., 2016. In-situ U–Pb dating and Nd isotopic analysis of perovskite from a rodingite blackwall associated with UHP serpentinite from southwestern Tianshan, China. Chem. Geol. 431, 67–82.

Siegesmund, S., Layer, P., Dunkl, I., Vollbrecht, A., Steenken, A., Wemmer, K., Ahrendt, H., 2008. Exhumation and deformation history of the lower crustal section of the Valstrona di Omegna in the Ivrea Zone, southern Alps. Geol. Soc. Lond., Spec. Publ. 298, 45–68.

Stacey, J., Kramers, J.D., 1975. Approximation of terrestrial lead isotope evolution by a two-stage model. Earth Planet. Sci. Lett. 26, 207–221.

van der Straaten, F., Halama, R., John, T., Schenk, V., Hauff, F., Andersen, N., 2012. Tracing the effects of high-pressure metasomatic fluids and seawater alteration in blueschist-facies overprinted eclogites: Implications for subduction channel processes. Chem. Geol. 292–293, 69–87. https://doi.org/10.1016/j.chemgeo.2011.11.008.

Sun, S., McDonough, W.F., 1989. Chemical and isotopic systematics of oceanic basalts: implications for mantle composition and processes. SP 42, 313–345. https://doi.org/10.1144/GSL.SP.1989.042.01.19.

Sun, J., Liu, C.-Z., Tappe, S., Kostrovitsky, S.I., Wu, F.-Y., Yakovlev, D., Yang, Y.-H., Yang, J.-H., 2014. Repeated kimberlite magmatism beneath Yakutia and its relationship to Siberian flood volcanism: Insights from in situ U–Pb and Sr–Nd perovskite isotope analysis. Earth Planet. Sci. Lett. 404, 283–295. https://doi.org/10.1016/j.epsl.2014.07.039.

Sun, J., Wu, F.-Y., Sklyarov, E., Sarkar, C., Liu, C.-Z., Pearson, G.D., Cheng, Z., Mitchell, R.N., 2022. Matrix effects during in situ U-Pb dating of perovskite with variable crystal structure: evidence from the Tazheran Massif, Russia. Chem. Geol. 589, 120685 https://doi.org/10.1016/j.chemgeo.2021.120685.

Tappe, S., Jenner, G.A., Foley, S.F., Heaman, L., Besserer, D., Kjarsgaard, B.A., Ryan, B., 2004. Torngat ultramafic lamprophyres and their relation to the North Atlantic Alkaline Province. Lithos 76, 491–518.

Tappe, S., Foley, S.F., Jenner, G.A., Heaman, L.M., Kjarsgaard, B.A., Romer, R.L., Stracke, A., Joyce, N., Hoefs, J., 2006. Genesis of ultramafic lamprophyres and carbonatites at Aillik Bay, Labrador: a consequence of incipient lithospheric thinning beneath the North Atlantic craton. J. Petrol. 47, 1261–1315.

Tappe, S., Foley, S.F., Kjarsgaard, B.A., Romer, R.L., Heaman, L.M., Stracke, A., Jenner, G.A., 2008. Between carbonatite and lamproite—diamondiferous Torngat ultramafic lamprophyres formed by carbonate-fluxed melting of cratonic MARID-type metasomes. Geochim. Cosmochim. Acta 72, 3258–3286.

Tappe, S., Pearson, D.G., Nowell, G., Nielsen, T., Milstead, P., Muehlenbachs, K., 2011. A fresh isotopic look at Greenland kimberlites: cratonic mantle lithosphere imprint on deep source signal. Earth Planet. Sci. Lett. 305, 235–248.

Toffolo, L., Nimis, P., Martin, S., Tumiati, S., Bach, W., 2017. The Cogne magnetite deposit (Western Alps, Italy): a late Jurassic seafloor ultramafic-hosted hydrothermal system? Ore Geol. Rev. 83, 103–126.

Trommsdorff, V., Evans, B.W., 1977. Antigorite-ophicarbonates: contact metamorphism in Valmalenco, Italy. Contrib. Mineral. Petrol. 62, 301–312.

Trommsdorff, V., Piccardo, G., Montrasio, A., 1993. From magmatism through metamorphism to sea floor emplacement of subcontinental Adria lithosphere during pre-Alpine rifting (Malenco, Italy). Schweiz. Mineral. Petrogr. Mitt. 73, 191–203.

Uher, P., Kodèra, P., Vaculovič, T., 2011. Perovskite from Ca-Mg skarn-porphyry deposit Vysoká Zlatno, Štiavnica stratovolcano, Slovakia. Mineral. Slovaca 43, 247–254.

Ulmer, P., Trommsdorff, V., 1995. Serpentine stability to mantle depths and subduction-related magmatism. Science 268, 858–861.

Vermeesch, P., 2018. IsoplotR: a free and open toolbox for geochronology. Geosci. Front. 9, 1479–1493. https://doi.org/10.1016/j.gsf.2018.04.001.

Vieira Duarte, J.F., Piccoli, F., Pettke, T., Hermann, J., 2021. Textural and geochemical evidence for magnetite production upon antigorite breakdown during subduction. J. Petrol. https://doi.org/10.1093/petrology/egab053.

Villa, I.M., Hermann, J., Müntener, O., Trommsdorff, V., 2000. 39 Ar– 40 Ar dating of multiply zoned amphibole generations (Malenco, Italian Alps). Contrib. Mineral. Petrol. 140, 363–381.

Vitale Brovarone, A., Alard, O., Beyssac, O., Martin, L., Picatto, M., 2014. Lawsonite metasomatism and trace element recycling in subduction zones. J. Metamorph. Geol. 32, 489–514. https://doi.org/10.1111/jmg.12074.

Vitale Brovarone, A., Martinez, I., Elmaleh, A., Compagnoni, R., Chaduteau, C., Ferraris, C., Esteve, I., 2017. Massive production of abiotic methane during subduction evidenced in metamorphosed ophicarbonates from the Italian Alps. Nat. Commun. 8, 14134. https://doi.org/10.1038/ncomms14134.

Vitale Brovarone, A., Sverjensky, D., Piccoli, F., Ressico, F., Giovannelli, D., Daniel, I., 2020. Subduction hides high-pressure sources of energy that may feed the deep subsurface biosphere. Nat. Commun. 11, 1–11. https://doi.org/10.1038/s41467-020-17342-x.

Vitale Brovarone, A., Piccoli, F., Frasca, G., Giuntoli, F., 2021. Fresh, pseudotachylite-bearing mantle peridotites from the lawsonite eclogite-facies San Petrone unit, Alpine Corsica. Ofioliti 46. https://doi.org/10.4454/ofioliti.v46i2.545.

Widom, E., Kepezhinskas, P., Defant, M., 2003. The nature of metasomatism in the sub-arc mantle wedge: evidence from Re–Os isotopes in Kamchatka peridotite xenoliths. Chem. Geol. 196, 283–306.

Wu, F.-Y., Yang, Y.-H., Mitchell, R.H., Li, Q.-L., Yang, J.-H., Zhang, Y.-B., 2010. In situ U–Pb age determination and Nd isotopic analysis of perovskites from kimberlites in southern Africa and Somerset Island, Canada. Lithos 115, 205–222.

Wu, F.-Y., Arzamastsev, A.A., Mitchell, R.H., Li, Q.-L., Sun, J., Yang, Y.-H., Wang, R.-C., 2013a. Emplacement age and Sr–Nd isotopic compositions of the Afrikanda alkaline ultramafic complex, Kola Peninsula, Russia. Chem. Geol. 353, 210–229.

Wu, F.-Y., Mitchell, R.H., Li, Q.-L., Sun, J., Liu, C.-Z., Yang, Y.-H., 2013b. In situ UPb age determination and SrNd isotopic analysis of perovskite from the Premier (Cullinan) kimberlite, South Africa. Chem. Geol. 353, 83–95.

Zhang, R., Yang, J., Wooden, J., Liou, J., Li, T., 2005. U–Pb SHRIMP geochronology of zircon in garnet peridotite from the Sulu UHP terrane, China: implications for mantle metasomatism and subduction-zone UHP metamorphism. Earth Planet. Sci. Lett. 237, 729–743.